2018

Nitrogen Rich Porous Organic Frameworks: Proton Conduction Behavior of 3D Benzimidazole and Azo-linked Polymers

Michael J. Anhorn
Virginia Commonwealth University

NITROGEN-RICH POROUS ORGANIC FRAMEWORKS: PROTON CONDUCTION

BEHAVIOR OF 3D BENZIMIDAZOLE AND AZO-LINKED POLYMERS

A thesis submitted in partial fulfillment of the requirements for the degree Master of Science at Virginia Commonwealth University.

by

Michael Justin Anhorn

Bachelors of Arts

University of North Carolina Wilmington, 2008

Director: Dr. Hani M. El-Kaderi,

Associate Professor, Department of Chemistry

Virginia Commonwealth University

Richmond, Virginia

May 2018

Acknowledgement

I would like to thank my research advisor, Dr. Hani M. El-Kaderi for giving me the opportunity to work under his supervision. Additionally, I would like to thank him for the patience that he has shown me over my 3 year tunure. I hope that he and I can maintain a professional and personal relationship moving forward. I would like to thank Dr. Oussama El-Kadri for his support and guidance and his soft touch with regards mentorship. Also, I would like to thank my colleagues at VCU, most importantly, my lab mates and Anna Forzano, Joshua Davis, and Christopher Ohlhaver. Additionally, Dr. Robert Giles has been extremely helpful to me on many different fronts. Lastly, I would like to thank Sarah Griffin for her continued support. Sarah saved and changed my life and for that, I am forever grateful.

Dedication

I would like to dedicate this work to my family for their continued support. More specifically, my mother, my brother, and my maternal grandparents. I am grateful for the sacrifices that were made on my behalf.

Table of Contents

Abstract

NITROGEN-RICH POROUS ORGANIC POLYMERS: THE EMERGENCE OF TWO

NEW CLASSES OF POLYMERS FOR USE AS PROTON EXCHANGE MEMBRANES

By Michael Justin Anhorn, MSc.

A thesis submitted in partial fulfillment of the requirements for the degree Master of Science at

Virginia Commonwealth University.

Virginia Commonwealth University, 2018.

Director: Dr. Hani M. El-Kaderi, Associate Professor, Department of Chemistry

Nitrogen-rich porous organic frameworks show great promise for use as acid-doped proton

conducting membranes, due to their high porosity, excellent chemical and thermal stability, ease

of synthesis, and high nitrogen content. Aided by very high surface area and pore volume, the

material has the ability to adsorb high amounts of H_3PO_4 into its network, which creates a proton

rich environment, capable of facile proton conduction. The morphology and chemical

environment, doping behavior, and proton conduction of these materials were investigated. With

such high acid-doping, *ex-situ* studies revealed that under anhydrous conditions, PA@BILP-16

(AC) produced a proton conductivity value of 5.8×10^{-2} S cm^{-1} at 60 °C and PA@ALP-6 showed

a slightly higher value of 5.91×10^{-2} S cm^{-1} at 60 °C. With such promising results, *in-situ*

experiments with various analogues are scheduled to be conducted in the near future.

Chapter 1

Introduction

1.1 Current Climatic Conditions

With current populations exceeding 7.5 billion and future population estimations expected to reach 10 billion by 2050, it is imperative to break the chains binding our society to an overwhelming reliance upon fossil fuels and move towards greener sources of energy.[1] Efforts do seem to be moving in the right direction with the World Energy Council reporting in their 2016 summary that there have been "unprecedented" changes in the world's energy consumption, with an "unexpected high growth in the renewables market.[2]" Figure 1.1 shows a graphical representation of the world energy consumption over the past 15 years.
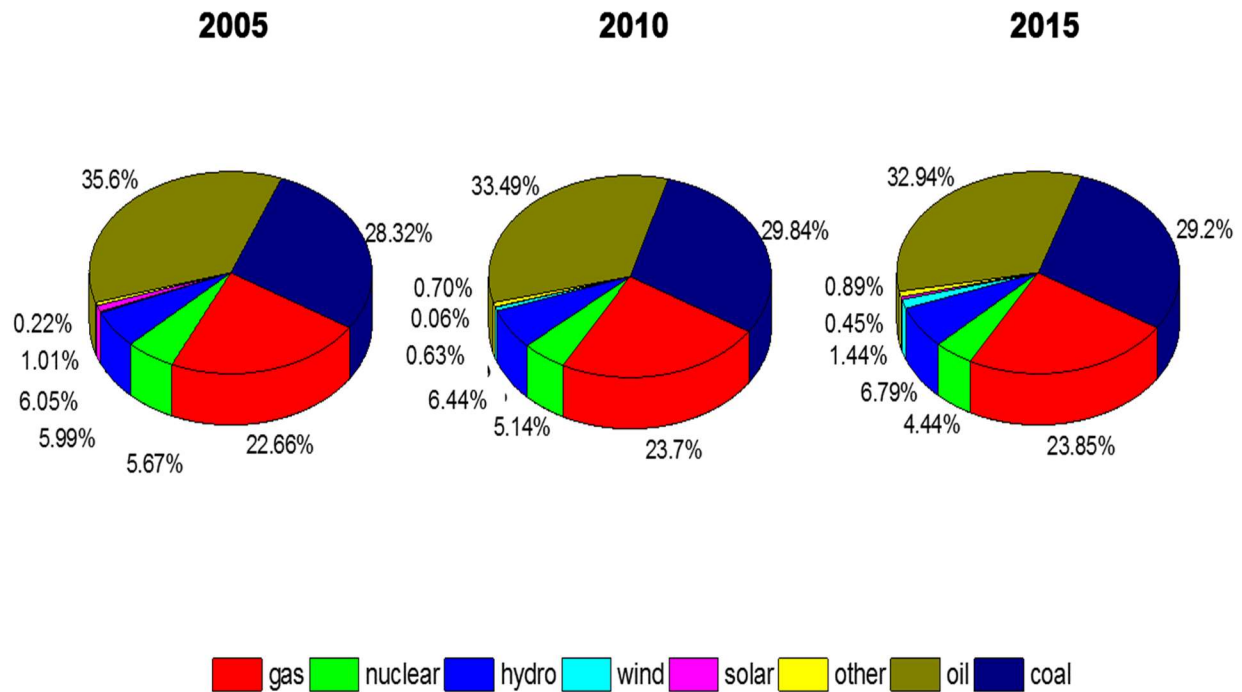
Figure 1.1 Graphical illustration of the world energy consumption by source since 2005.[2]

Even with these unprecedented changes, the energy market share for coal, natural gas, and oil easily surpasses 80%.[2] The three most prominent alternatives to fossil fuels are hydro, nuclear, and wind power, but tout a mere 6.79%, 4.44%, and 1.44 % of the energy market share in 2015, respectively.[2] Alternative options to traditional sources of energy come with limiting factors, i.e. the overwhelming cost, safety issues, waste disposal issues, and the public's negative view. If our reliance upon environmentally harmful energy sources is to be overcome, efforts to alleviate the above aforementioned issues and to tackle the other challenges facing the research community must take a central focus.

1.2 Energy Sources

There are three main categories of energy resources: fossil fuels, nuclear resources, and renewable energy resources.[3] Figure 1.2 gives a breakdown of the mainstream energy resources. With an astounding 86% of world energy sources comprised of fossil fuels, we have seen
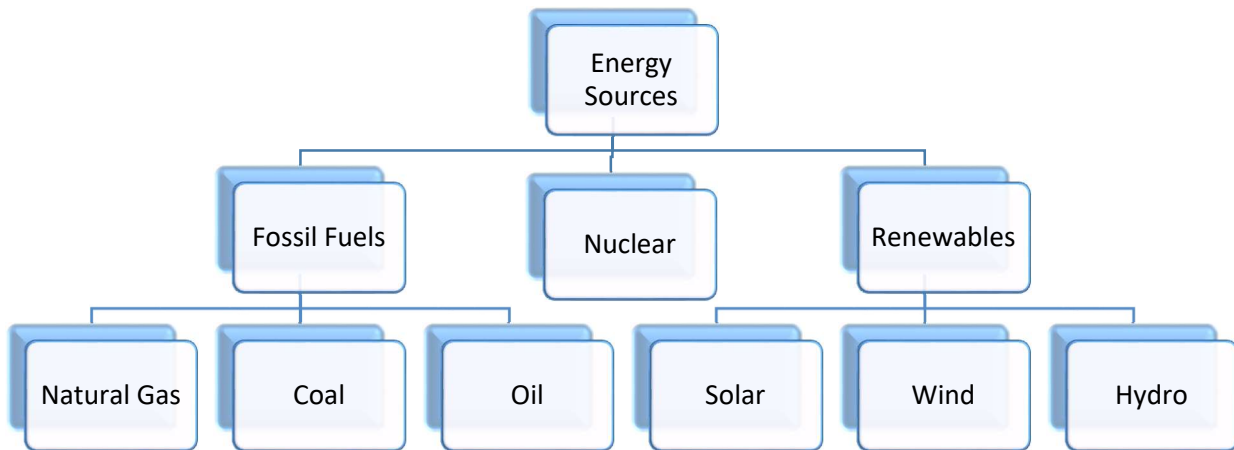
Figure 1.2 Diagram of current mainstream energy resources.

a dramatic increase in CO_2 levels in the atmosphere from 280 ppm to 390 ppm during the preindustrial era to now.[4] In order to counter this current trend, there needs to be a stronger reliance upon renewable energy sources that do not add to the CO_2 levels in the atmosphere.

1.3 Fuel Cell Technology

A technology that is not yet considered mainstream, but that has promise to establish itself as a leading contributor to the alternative energy realm, is fuel cell technology. This is not a new concept, with the first fuel cell immerging in 1838. This technology was composed of platinum plates, porous materials, sulfuric acid, and hydrogen gas and air.[5] This work, termed "gas batteries," draws upon earlier work by Humphry Davy and Christian Friedrich Schönbein and was subsequently improved upon by Mond and Langer, creating the first working fuel cell.[6] Fuel cells are still limited in use due to life time and cost.[7-8] Table 1.1 makes a comparison between fuel cell technology, solar energy, and wind power.[8]

Technology	Capacity Factor	Life (years)	Payback (years)	CO_2 emission reduction (kg)
Fuel Cell	95	20	7.9	979,526
Wind	17.5	25	36.5	268,175
Solar	25.8	20	8	539,954

Table 1.1 Comparison between fuel cell, wind, and solar energy sources.[8]

As can be seen from Table 1.1, fuel cell technology strongly competes with these two mainstream alternate energy resources.

1.3.1 Types of Fuel Cells

Fuel cell technology has received considerable attention since its origination in the 19th century and there have been many variations created. Although there are many different types of fuel cells, the premise is still the same: convert chemical energy (stored) into electrical energy. There are

five main types of fuel cells: proton exchange membrane fuel cells (PEMFCs), direct methanol fuel cells (DMFCs), solid oxide fuel cells (SOFCs), molten carbonate fuel cells (MCFCs), and alkaline fuel cells (AFCs). Table 1.2 lists the different types of fuel cells, the materials from which they are typically made, the operating temperatures, and the advantages and disadvantages.[9-10]

FC Type	Common Electrolyte	Operating Temperature	Advantages	Disadvantages
PEM	Perfluorosulfonic Acid	50-100 °C	Low temperature Quick starup	Expensive catalysts
Alkaline (AFC)	KOH soaked in a matrix	90-100 °C	Low cost components	CO_2 sensitivity
Phosphoric Acid (PAFC)	PA soaked in a matrix	150-200 °C	Increased fuel tolerance	Expensive catalysts
Molten Carbonate (MCFC)	Solution of metal carbonates soaked in a matrix	600-700 °C	High efficiency Fuel flexibility	Breakdown of components Low power density
Solid Oxide (SOFC)	Yttria-stabilized zirconia	700-1000 °C	High efficiency Fuel Flexibility	Long start up Breakdown of components

Table 1.2 Comparison of Fuel Cell Technologies.[9,10]

Out of the five types, alkaline fuel cells have been most extensively studied due to the enhanced kinetics of the oxygen reduction reaction (ORR) created by the alkaline rich environment.[11] Additionally, this type of fuel cell employs non-noble metals as catalytic materials, which helps alleviate some of the overhead towards mass production. AFCs have not seen wide spread commercialization due to the use of liquid electrolytes that result in two main problems.[12] First is the production of carbonate that occurs from the reaction of hydroxide ions and carbon dioxide from the air, which leads to a reduction in hydroxide ion concentration and may cause blockage of

the porous electrodes (precipitation of carbonate).[13-15] Secondly, liquid electrolyte management poses a huge disadvantage.[16-17] Due to improvements in technology and its advantages over other types of fuel cells, there has been a huge resurgence in PEMFC research. Of the various types, proton exchange membrane fuel cells (PEMFCs) show the most promise and are most feasible for wide spread commercialization.

1.4 Proton Exchange Membrane Fuel Cells (PEMFCs)

The first PEMFC was created by Tom Grubs and General Electric in 1954 with DuPont subsequently improving upon their work and designing a membrane composed of a pefluoronated polymer with sulfonated side chains.[18-19] Figure 1.3 gives the structure of DuPont's membrane, coined Nafion®.
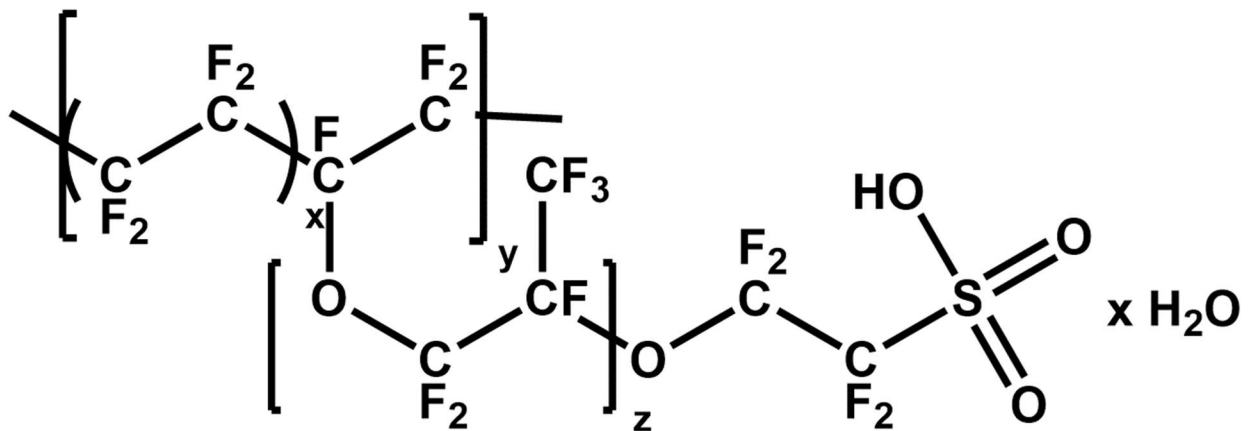
Figure 1.3 Chemical Structure of Nafion®

Nafion® has remained the golden standard since its development in the 1970s, but it comes with its own inherent challenges. These challenges limit its use to low temperature polymer electrolyte membrane fuel cells (LT-PEMFCs).

Proton exchange membrane fuel cells are promising alternatives to current technologies such as the combustion engine and other non-renewable resources. The benefits of PEMFCs make them more viable for large-scale production than current mechanical technologies. This fact has led to a recent resurgence of efforts to improve the current technology and create innovative materials.[9,20-25]

1.4.1 Proton Exchange Membrane Fuel Cell Components

Proton exchange membrane fuel cells can range in size from a single unit to multiple units connected in series. In 2014, Solvay successfully commissioned a 1 Megawatt (MW) industrial fuel cell, the world's largest PEMFC.[26] This joint venture commanded a whopping 17.3-million-dollar budget.[26] Most fuel cells do not match this scale, but all are composed of similar components and hardware. The heart of the PEMFC is the membrane electrode assembly (MEA), which is composed of two catalyst layers (anode and cathode) and the proton exchange membrane. The rest of the setup depends on the application, but it is typical to incorporate gas diffusion layers, current collector plates, and a set of bipolar plates. Figure 1.4 depicts the main components of a single stack fuel cell and gives a simple illustration of the transformation of chemical energy into electrical energy.
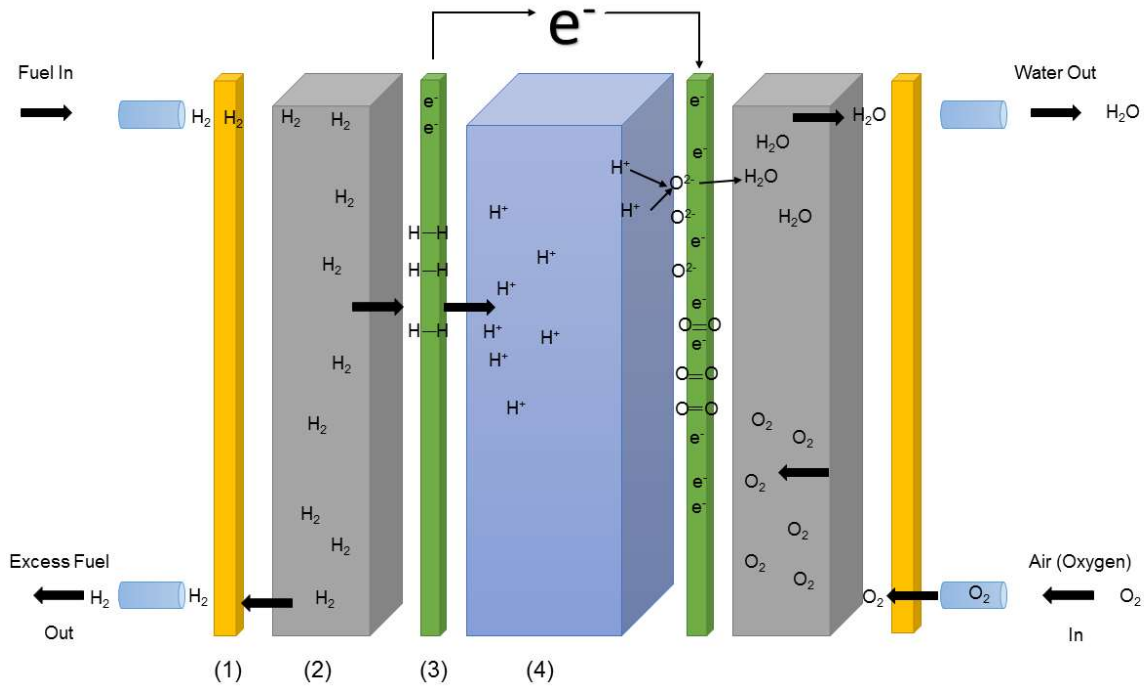
Figure 1.4 Illustration of the components of a single-stack PEMFC.

The current collector plates (1) play a simple role in the overall setup, with two main objectives. First, these plates help hold the assembly together, typically using a through bolt assembly. Secondly, they connect the unit to the external load and if properly equipped, they can facilitate heat management for the cell. The bipolar plates (2), or separator plates, play a more significant role with multiple functions. The separator plates must be able to distribute the fuel and oxidant throughout the cell, separate individual cells within the stack, and facilitate water management.[27] The importance of each function must be taken into account (per application) and thus, the materials that these are manufactured from must be tailored to that particular application. The materials that have received attention can be broadly placed into three categories: non-metal, non-porous graphite, metals: coated and non-coated, and composites: polymer-metal and polymer-carbon.[27] The separator plates are typically connected to the MEA using a gasket and a gas

diffusion layer. The membrane electrode assembly consists of three components: the two catalyst layers (3) (anode and cathode) and the membrane (4). The MEA is fabricated using the "catalyst-coated gas diffusion layer (CCG)" or the "catalyst-coated membrane (CCM)" method, which is typically applied through a spray-coating method.[28] The role of the catalyst layer is to facilitate the hydrogen evolution reaction (HER) at the anode and the oxygen reduction reaction (ORR) at the cathode. Equations 1-3 show the half reactions at the anode (Equation 1) and cathode (Equation 2), as well as the overall chemical equation (Equation 3).

$$H_2 \rightarrow 2H^+ + 2e^- \tag{1}$$

$$O_2 + 4e^- \rightarrow 2O^{2-} \tag{2}$$

$$2H_2 + O_2 \rightarrow 2H_2O \tag{3}$$
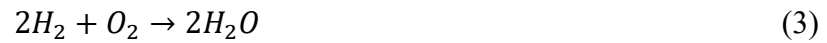
The most commonly employed catalyst is Pt-based, but much research is underway to develop novel catalysts that utilize non-noble metals.

The central element to the MEA is the proton exchange membrane. The most important role of PEMs is quick and facile proton mediation from the anode to the cathode. Additionally, the membrane must act as a barrier between reactant gases (preventing fuel crossover), a support for MEA construction, an electrical insulator and possess adequate chemical and thermal stability, along with high durability and mechanical strength.[20] Finally, solid polymer electrolyte membranes (SPE) must exhibit dimensional and morphological stability, adequate water and waste transport properties, long term operational stability under harsh conditions, and low cost.[9] In an

attempt to capture as many of these functions as possible, research in this arena has exploded and novel materials with different chemical and physical properties have been investigated.

1.4.2 Polymer Electrolyte Membranes: Materials

There has been an extensive effort to improve upon the work by DuPont and many perfluorosulfonated-based membranes have been developed. Due to the limitations of membranes composed of Naftion-type solid polymer electrolytes, materials including, but not limited to, polystyrene-based membranes,[29-30] sulfonated polyimide (SPI)-based membranes,[31-32] polybenzimidazole (PBI)-based membranes,[35-36] and polyphosphazene-based membranes.[33-34] have been explored. More recently, with the discovery of materials with intrinsic porosity, MOFs and COFs, there has been an explosion of research using these materials as acid-doped proton exchange membranes.

Nafion® and Naftion-type Membranes

As previously mentioned, Nafion® has remained the benchmark in PEMFCs for over 40 years. This has been possible due to many factors, including Nafion's high proton conductivity and excellent oxidative and chemical stability, which arises from its structural similarities to another DuPont-made compound, Teflon.[9] Nafion membranes can obtain proton conductivity values on the order of 0.07-0.08 S cm^{-1} at room temperature under fully hydrated conditions.[37] The chemical structure shown in Figure 1.3, lends clarity to why Nafion shows such high conductivity values. The backbone of the polymer is sulfonated, which leads to two distinct regions, the hydrophilic region, where the water molecules migrate and hydrophobic regions that are not part of the proton mediation pathway. As the membranes becomes hydrated, the water molecules begin to form

clusters around the sulfonated regions and as these clusters grow, a larger separation between hydrophobic and hydrophilic regions form, which lends to formational, dimensional, and connective control of the proton conduction pathways.[9,38,39]

Although many studies have shown Nafion to exhibit such high proton conductivity values, it is beset by many challenges. Mainly, the membrane shows extremely low conductivity values under low humidity and anhydrous conditions and thus, these membranes are limited to applications that use LT-PEMFCs. Under optimum fuel cell operating conditions, humidity management becomes an issue. This leads to continuous monitoring of water content to prevent flooding, which ultimately lowers efficiency.[25,26] Aside from evaporation issues, operation at elevated temperatures causes instability within the membrane due to the loss of sulfonic acid groups.[40] Additionally, fabrication of membrane electrode assemblies (MEAs) become extremely costly when incorporated with Nafion type membranes. With Nafion's performance being limited to certain undesirable conditions, alternative materials for commercialization are necessary.

Polystyrene-based, Polyphosphazene-based, and Sulfonated Polyimide-based membranes

Polystyrene-based membranes were the first to be commercialized and were developed by GE in 1955.[9] Unfortunately, production was short lived due to degradation problems caused by moderate to high temperatures; loss of styrene sulfonated acid groups are observed under fuel cell operating conditions at a detrimental rate of up to 0.1% per hour.[9,41-42] In an attempt to circumvent degradation issues caused by higher temperatures, sulfonated polyimide-based membranes were investigated, which possess high thermal and mechanical properties and a durability against aggressive chemicals.[9] Figure 1.5 gives an example of SPI-based materials used in proton conductive membranes. The first generation of SPI-based membranes showed low conductivity

with values bewtween 2 x 10^{-3} to 4 x 10^{-2} S/cm,[43,44] but the second generation of materials were greatly improved and exhibited conductivity values that compete with Nafion® (1.67 S/cm).[45] Although these results began to excite researchers, issues such as hydrolytic stability, oxidative
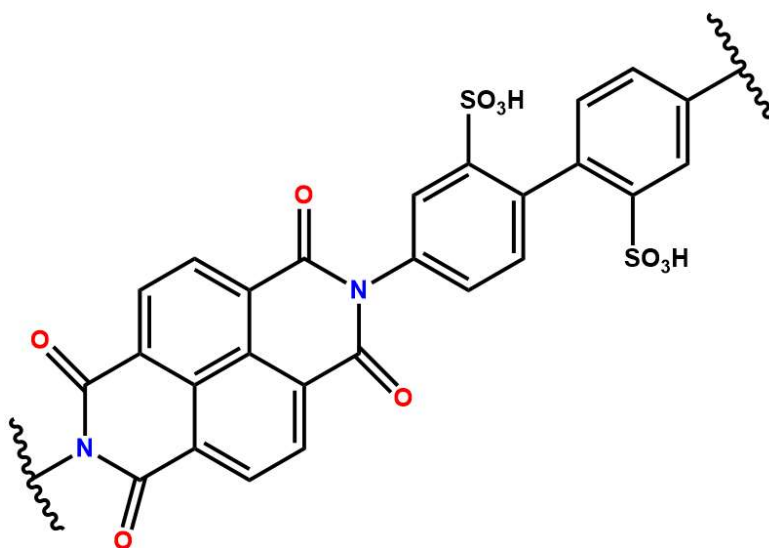
Figure 1.5 Napthalenic sulfonated polyimide.

stability, and swelling-stress stability prevent these materials from reaching mass production.[9] Another interesting group of materials are polyphosphazenes. Figure 1.6 gives a simple synthetic procedure for making polyphosphazenes. The chloride groups can be easily exchanged for phosphorous and nitrogen atoms and organic, inorganic, or organometallic side groups, making these materials extremely versatile.[9] Although these materials can be easily tuned to give specific mechanical and chemical properties, they are limited by insufficient research.
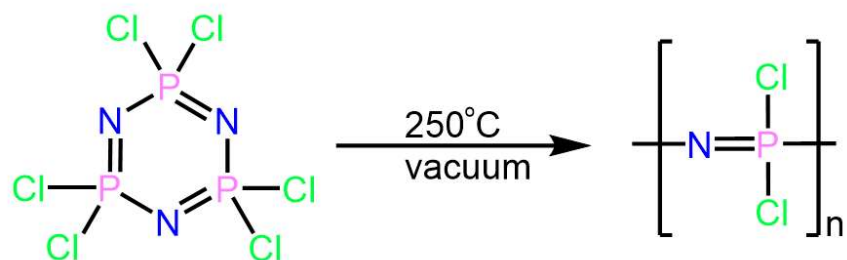
Figure 1.6 Synthetic procedure for polymerization of phosphazene.

Metal Organic Framework-based Membranes

Metal organic frameworks (MOFs), also known as porous coordination polymers (PCPs), were first developed by Omar Yaghi in 1995.[48] These materials are composed of a metal center (secondary building unit) and organic linkers. MOFs are extremely attractive due to the synthetic approaches that allow for specific topology that can be tailored to particular applications. Additionally, these materials can be post-modified to incorporate different molecular groups that can enhance chemical and physical properties. These qualities have caused many research groups to investigate their use in such applications as gas storage/separation,[49-51] catalysis,[52-54] and guest molecule encapsulation.[55,56] Due to the tailorable structures/properties, crystallinity, and porosity, MOFs are strong candidates for solid electrolyte proton conducting materials. MOFs have been investigated for proton conduction applications utilizing water-mediated proton conductivity and guest/host interactions. These materials have exhibited high proton conductivity values, reaching

levels up to 10^{-1} S/cm under highly humidified conditions by incorporating sulfate, amine, phosphate, and carboxylate groups.[57-60] Fuel crossover issues and instability under fuel cell conditions prevent these types of materials from reaching commercialization.[61]

Covalent Organic Framework-based Membranes

Subsequently, materials similar to MOFs were created using analogous strategies, but with one main difference, the absence of metal secondary building units. Covalent organic frameworks (COFs), also known as porous organic polymers (POPs), are constructed solely from organic linkers and by creating these materials through covalent bonding, superior long-term stability can be achieved.[62] Additional advantages of COFs over MOFs include greener and lighter weight materials, while retaining crystallinity, porosity, and tuneability. Research in the area of covalent organic frameworks have mostly been limited to gas storage, catalysis, and photoconductivity.[63-65] Recenlty, Rahul Banerjee *et al.* created a covalent organic frameworks based upon the Schiff base reaction termed, TpPa-2 that showed chemical stability in up to 9 N HCl and 9 N NaOH.[67] These findings led this group to subsequently study an azo-linked material based upon similar starting materials and that was synthesized through a similar procedure for use in fuel cell applications.[66] It was found that by anchoring phosphoric acid to the basic azo sites, high proton conductivity, 9.9 x 10^{-4} under nearly fully hydrated conditions, could be achieved.[66] Two years later, the same group reported a new material, based on one of the same monomers used in previous publications (Tp (1,3,5-triformylphloroglucinol)), that displayed intrinsic proton conductivity through sulfonic acid groups.[61] The material was further modified to incorporate pyridine into the structure, creating a basic site that could immobilize acidic proton carriers and allow for both intrinsic proton conduction through the sulfonic sites and extrinsic proton conduction through the

immobilized acid with labile protons.[61]   The proton conductivity value for TpPa-SO$_3$H under anhydrous conditions was reported as 1.7 x 10^{-5} S/cm at 120 °C and the conductivity value for the pyridine-modified analogue TpPa-SO$_3$H-Py reached 5 x 10^{-4} S/cm at 120 °C. This pioneering work has led others to investigate COFs for use in fuel cell applications,[68,69] but work in this area is extremely limited and further research should be conducted.

Polybenzimidazole-based Membranes

The concept for PBI-based membranes originated from trying to solve the disadvantages of phosphoric acid-based fuel cells that employed a liquid electrolyte "trapped" in a silicon carbide ceramic-type matrix.[46-47] There was a need for an improved matrix for phosphoric acid that acted on chemical interactions to prevent leakage of H$_3$PO$_4$, instead of common macroporous networks that relied solely upon capillary action.[9] Polymers that can participate in Lewis acid/base interactions through the basic regions of the polymer are extremely attractive because they can form poly salt systems capable of facilitating proton conduction.   Figure 1.7 shows these interactions on the molecular scale for a single benzimidazole moiety.
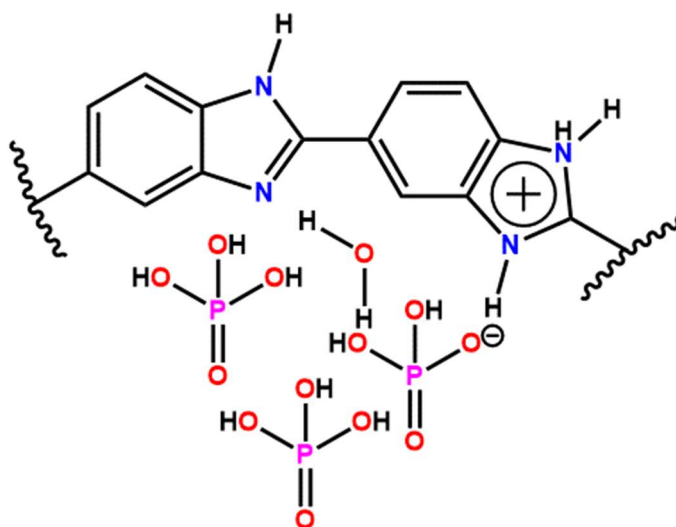
Figure 1.7 Interaction between a phosphoric acid species and a benzimidazole moiety.

Of the materials that can participate in these acid/base interactions, polybenzimidazole and its derivatives are of great interest due to their stability in harsh conditions. Many different acids have been employed, but phosphoric acid have received much attention due to its amphoteric nature, high proton conductivity, and thermal stability.

Benzimidazole Linked Polymer-based and Azo Linked Polymer-based Membranes

A unique class of porous organic polymers was developed by the El-Kaderi group, which utilizes a metal-free condensation reaction between an aryl-o-diamine and aryl-aldehyde, leading to the formation of imidazole linkages.[70] This metal-free synthetic route is of interest due to the elimination of metal trapping and the absence of a metal catalyst minimizing production costs.[71] The lightweight nature, high porosity, high nitrogen content, and structural tuneability of these

materials make them extremely attractive for many applications, but to date, benzimidazole-linked polymers have only been investigated in two main areas: (i) gas storage and (ii) gas separation.[72-74] It has been shown that by changing the building blocks, the physical and chemical properties of these materials are effectively changed. The work by the El-Kaderi group has shown that the surface area and functionality of these materials play a huge role in gas uptake. More recently, Tsemre Tessema *et al.* investigated the use of two polymers of this type for use in mixed matrix membranes (MMM) with flue gas separation applications in mind.[75] In this work, the authors were able to successfully develop a defect-free MMM that showed excellent thermal stability, but was somewhat limited in performance. This suggests that there is more work to be done in this area of research, in addition to utilizing BILPs for use in other uncharted areas of research.

Another new class of polymers bearing an azo-linkage was recently reported by two groups.[76-79] These materials show excellent chemical and thermal stability coupled with high CO_2 uptake, which make them strong candidates for carbon dioxide capture and storage. Work by Patel *et al.* showed very high CO_2/N_2 selectivity (up to 131 at 298 K) for azo-linked covalent organic polymers (azo-COPs), but showed low CO_2 uptake capacities, which limits their applicability.[77,80] Azo-COPs are limited in carbon dioxide capture due to their relatively low porosities, but azo-linked polymers (ALPs) exhibit high porosities and high levels of carbon dioxide uptake.[80] Although research has been limited to gas separation and gas uptake applications, the properties that make them appealing for these applications (high porosity, high nitrogen content, and high thermal and chemical stability) make these materials great candidates for other applications, such as proton conducting membranes.

Introduction References

1. World Population Prospects
   https://esa.un.org/unpd/wpp/Publications/Files/WPP2017_KeyFindings.pdf (accessed Apr
   25, 2018).

2. World Energy Resources https://www.worldenergy.org/wp-
   content/uploads/2016/10/World-Energy-Resources-Full-report-2016.10.03.pdf (accessed
   Apr 25, 2018).

3. Demirbas A. Recent advances in biomass conversion technologies. *Energy Educ Sci
   Technol*. **2000**, *6*, 19–40.

4. Earth System Research Laboratory. Global Monitoring Division. National Oceanic and
   Atmospheric Administration. U.S. Department of Commerce; 2005.

5. *Philosophical Magazine and Journal of Science* 1843

6. Improvements in Gas Batteries. I,. Mond, Northwich, and C. Langer, London. Eng. Pat.
   241 1, February 17, 1888. 8rf.

7. Satyapal, S.; Petrovic, J.; Read, C.; Thomas, G.; Ordaz, G. *Catalysis Today*. **2007**, *120*,
   246-256.

8. Dasa, V.; Padmanabanb, S.; Venkitusamya, K.; Selvamuthukumaranc, R.; Blaabjergd, F.;
   Sianoe, P. *Renewable and Sustainable Energy Reviews*. **2017**, *73*, 10-18.

9. Kravtsberg, A.; Ein-Eli, Y. *Energy Fuels*. **2014**, *28*, 7303-7330.

10. Fuel Cell Technologies Program

    https://www1.eere.energy.gov/hydrogenandfuelcells/fuelcells/pdfs/fc_comparison_chart.pd

    f (accessed Apr 25, 2018).

11. Pan, Z.F.; Ana, L.; Zhao, S.; Z.K. Tang. *Progress in Energy and Combustion Science*.

    2018, *66*, 141-175.

12. Merle, G.; Wessling, M.; Nijmeijer, K. *J. Membrane Sci.* **2011**, *377*, 1-35.

13. Gulzow, E.; Schulze, M. *J. Power Sources*. **2004**, *127*, 243-251.

14. McLean, G.F.; Niet, T.; Prince-Richard, S.; Djilali, N.; *J. Hydrogen Energy*. **2002**, *27*, 507-

    526.

15. Gouerec, P.; Poletto, L.; Denizot, J.; Sanchez-Cortezon, E.; Miners, J.H. *J. Power Sources*.

    2004, *129*, 193-204.

16. Wang, Y.J.; Qiao, J.L.; Baker, R.; Zhang, J. *J. Chem Soc Rev*. **2013**, *42*, 5768-5787.

17. Li, Y.S.; Zhao, T.S.; Chen, R. *J. Power Sources*. **2011**, *196*, 133-139.

18. The Evolution of the PEM Stationary Fuel Cell in the U.S. Innovation System.

    http://www.oecd.org/science/inno/31967874.pdf

19. Grot, W. *Chem. Ing. Tech.* **1972**, *44*, 167.

20. Zhang, Y.; Li, J.; Ma, L.; Cai, W.; Cheng, H. *Energy Technology*. **2015**, *3*, 675-691.

21. Caretta, N.; Tricoli, V.; Picchioni, F. *J. Membrane Sci.* **2000**, *166*, 189-197.

22. Savadogo, O.J. *New Mater. Electroche. Syst.* **1998**, *1*, 47.

23. Homberg, S.; Lehtinen, T.; Nasman, J.; Ostrovskii, D.

24. Vallejo, E.; Pourcelly, G.; Gavach, C.; Mercier, R.; Pineri, M. *J. Membr. Sci.* **1999**, *160*, 127

25. Woo, Y.; Oh, S. Y.; Kang, Y. S.; Jung, B. *J. Membr. Sci.* **2003**, *220*, 31

26. Solvay https://www.solvay.com/en/media/press_releases/20120206-fuelcell.html (accessed Apr. 25, 2018).

27. Hermann, A.; Chaudhuri, T.; Spagnol, P. *International J. of Hydrogen Energy*. **2005**, *30*, 1297-1302.

28. Kim, G.H.; Eom, K.S.; Kim, M.; Yoo, S.J.; Jang, J. H.; Kim, H.; Cho, E.; *ACS Appl. Mater. Interfaces*. **2015**, *7*, 27581-27585.

29. Grubb, W.T., Jr. U.S. Patent 2,913,511 19550

30. Grubb, W.T.; Niedrach, L.W. *j. Electrochem. Soc.* **1960**, *107*, 131.

31. Hickner, M.A.; Ghassemi, H.; Kim, Y.S.; Einsla, B.R.; McGrath, J.E. *Chem. Rev.* **2004**, *104*, 4587.

32. Zhang, H.; Shen, P.K. *Chem. Rev.* **2012**, *112*, 2780.

33. Wycisk, R.; Pintauro, P.N. *J. Membr. Sci.* **1996**, *119*, 155.

34. Allock, H.R.; Fitzpatrick, R.J.; Salvati, L. *Chem. Mater.* **1991**, *3*, 1120.

35. Qingfeng, L.; Hjuler, H.A.; Bjerrum, N.J. *J. Appl. Electrochem.* **2001**, *31*, 773.

36. Yang, J.S.; Cleemann, L.N.; Steeenberg, T.; Terkelsen, C.; Li, Q.F.; et al. *Fuel Cells*. **2014**, *14*, 7.

37. *J. Electrochem. Soc.* **1996**, *143*.

38. Halim, J.; Bü chi, F. N.; Haas, O.; Stamm, M.; Scherer, G. G. *Electrochim. Acta* **1994**, *39*, 1303.

39. Kreuer, K.-D. *Chem. Mater*. **1996**, *8*, 610.

40. Mondal, A. N.; Tripathi, B.P.; Shahi, V.K. *J. Mater. Chem.* **2011**, *21*, 4117-4124.

41. Carretta, N.; Tricoli, V.; Picchioni, F. *J. Membr. Sci.* **2000**, *166*, 189.

42. Ahmed, M.; Dincer, I. *Int. J. Energy Res.* **2011**, *35*, 1213.

43. Vallejo, E.; Pourcelly, G.; Gavach, C.; Mercier, R.; Pineri, M. *J. Membr. Sci*. **1999**, *160*, 127.

44. Woo, Y.; Oh, S. Y.; Kang, Y. S.; Jung, B. *J. Membr. Sci*. **2003**, *220*, 31.

45. Miyatake, K.; Zhou, H.; Uchida, H.; Watanabe, M. *Chem. Commun*. **2003**, *368.*

46. Sammes, N.; Bove, R.; Stahl, K. Curr. Opin. *Solid State Mater. Sci*. **2004**, *8*, 372.

47. Carrette, L.; Friedrich, K. A.; Stimming, U. *Fuel Cells.* **2001**, *1*, 5.

48. Yaghi,O.M.;Li, G.; Li, H. *NatureI. 1995, 378.* 703.

49. Herm, Z.R.; Bloch, E.D.; Long, J.R. *Chem. Mater.* **2014**, *26*, 323.

50. Sumida, K.; Rogow, D.L.; Mason, J.A.; McDonald, T.M.; Bloch, E.D., Herm, Z.R.; Bae, T.H.; Long, J.R. *Chem. Rev.* **2012**, *112*, 724.

51. Li, Y.W.; Xu, J.; Li, D.C.; Dou, J.M.; Yan, H.; Hu, T.L.; Bu, X.H. *Chem Commun.* **2015**, *51*, 14211.

52. Farrusseng, D.; Aguado, S.; Pinel, C. *Angew. Chem. Int. Ed.* **2009**, *48*, 7502.

53. Corma, A.; Garcia, H.; Xamena, F. *Chem Rev.* **2010**, *110*, 4606.

54. Fang, Z.L.; Bueken, B.; De Vos, D.E.; Fischer, R.A. *Angew. Chem. Int. Ed.* **2015**, *54*, 7234.

55. Wang, H.; Xu, J.; Zhang, D.S.; Chen, Q.; Wen, R.M.; Chang, Z.; Bu, X.H. *Angew. Chem. Int. Ed.* **2015**, *54*, 5966.

56. Jia, Y.Y.; Zhang, Y.H.; Xu, J.; Feng, R.; Zhang, M.S.; Bu, X.H. *Chem. Commun.* **2015**, *51*, 17439.

57. Tu, T.N.; Phan, N.Q.; Vu, T.T.; Nguyen, H.L.; Cordova, K.E.; Furukawa, H. *J. Mater. Chem. A.* **2016**, *4*, 3638.

58. Yang, F.; Huang, H.L.; Wang, X.Y.; Li, F.; Gong, Y.H.; Zhong, C.L.; Li, J.R. *Cryst. Growth Des.* **2015**, *15*, 5827.

59. P. Ramaswamy, N.E. Wong, B.S. Gelfand, G.K.H. Shimizu, *J. Am. Chem. Soc.* **2015**, *137*, 7640.

60. Nguyen, N.T.T.; Furukawa, H.; Gandara, F.; Trickett, C.A.; Jeong, H.M.; Cordova, K.E.; Yaghi, O.M. *J. Am. Chem. Soc.* **2015**, *137*, 15394.

61. Chandra, S.; Kundu, T.; Dey, D.; Addicoat, M.; Heine, T.; Banerjee, R. *Chem. Mater.* **2016**, *28*, 1489-1494.

62. Kang, D. W.; Song, J.H.; Lee, K.J.; Lee, H.G.; Kim, J.E.; Lee, H.Y.; Kim, J.Y.; Hong, C.S. *J. Mater. Chem. A.* **2017**, *5*, 17492-17498.

63. Huang, N.; Chen, X.; Krishna, R.; Jiang, D. *Angew. Chem., Int. Ed.* **2015**, *54*, 2986−2990.

64. Ding, S. Y.; Gao, J.; Wang, Q.; Zhang, Y.; Song, W.; Su, C.; Wang, W. *J. Am. Chem. Soc.* **2011**, *133*, 19816−19822.

65. Dogru, M.; Handloser, M.; Auras, F.; Kunz, T.; Medina, D.; Hartschuh, A.; Knochel, P.; Bein, T. *Angew. Chem., Int. Ed.* **2013**, *52*, 2920− 2924.

66. Chandra, S.; Kundu, T.; Kandambeth, S.; BabaRao, R.; Marathe, Y.; Kunjir, S.; Banerjee, R. *J. Am. Chem. Soc.* **2014**, *136*, 6570-6573.

67. Kandambeth, S.; Mallick, A.; Lukose, B.; Mane, M.; Heine, T.; Banerjee, R. *J. Am. Chem. Soc.* **2012**, *134*, 19524-19527.

68. Montoro, C.; Rodriguez-San-Miguel, D.; Polo, E.; Escudero-Cid, R.; Ruiz-Gonzalez, M.L.; Navarro, J.A.R.; Ocon, P.; Zamora, F. *J. Am. Chem. Soc.* **2017**, *139*, 10079-10086.

69. Peng, Y.; Xu, G.; Hu, Z.; Cheng, Y.; Chi, C.; Yuan, D.; Cheng, H.; Zhao, D. *ACS Appl. Mater. Interfaces*. **2016**, *8*, 18505-18512.

70. Rabbani, M. G.; El-Kaderi, H. M. *Chemistry of Materials.* **2011**, *23*, 1650-1653.

71. Sekizkardes, A.K. PhD. Dissertation, Virginia Commonwealth University, 2014.

72. Rabbani, M. G.; El-Kaderi, H. M. *Chemistry of Materials.* **2012**, *24*, 1511-1517

73. Rabbani, M. G.; Reich, T. E.; Kassab, R. M.; Jackson, K. T.; El-Kaderi, H. M. *Chem. Commun.* **2012**, *48*, 1141-1143.

74. Rabbani, M. G.; Sekizkardes, A. K.; El-Kadri, O. M.; Kaafarani, B. R.; El-Kaderi, H. M. *J. Mater. Chem.* **2012**, *22*, 25409-25417.

75. Tessema, T.D.M.; Venna, S.R.; Dahe, G.; Hopkinson, D.P.; El-Kaderi, H.M.; Sekizkardes, A.K. *Journal of Membrane Science*. **2018**, *554*, 90-96.

76. Arab, P.; Rabbani, M. G.; Sekizkardes, A. K.; İslamoğlu, T.; El-Kaderi, H. M. *Chemistry of Materials*. **2014**, *26*, 1385-1392.

77. Patel, H. A.; Je, S. H.; Park, J.; Chen, D. P.; Jung, Y.; Yavuz, C. T.; Coskun, A. *Nature Communications*. **2013**, *4*, 1357.

78. Lu, J.; Zhang, J. *Journal of Materials Chemistry A*. **2014**, *2*, 13831-13834.

79. Patel, H. A.; Je, S. H.; Park, J.; Jung, Y.; Coskun, A.; Yavuz, C. T.*Chemistry – A European Journal*. **2014**, *20*, 772-780.

80. Arab, P. PhD. Dissertation, Virginia Commonwealth University, 2015.

Chapter 2

Benzimidazole-Linked Polymer-Based Proton Exchange Membranes

2.1 Introduction

Porous materials have gained a lot of attention over the past two decades, with most research involving gas storage and gas separation,[1-3] catalysis,[4-6] and guest molecule encapsulation.[7,8] The properties that make these materials suitable for these applications, also make them attractive for use in acid-doped proton conducting materials. High surface area and pore volume, functionality, ease of synthesis, high chemical and thermal stability, and high nitrogen content make BILPs strong candidates for acid-doped polymer electrolyte membranes. Building upon the pioneering work done by Banerjee *et al.*[9,10] and taking into account previous work done with linear benzimidazole-based materials,[11] this project aimed to incorporate the most promising characteristics of these materials, while limiting their inherent disadvantages.

2.2 Experimental Procedures

Materials

All solvents and starting materials were purchased from Acros Organics or Sigma-Aldrich, unless otherwise specified, and used without further purification. 3,3′-diaminobenzidine tetrahydrochloridehydrate was purchased from Acros Organics.

Synthesis of BILP-16 (AC)

BILP-16 (AC) and 1,2,4,5-tetrakis(4-formylphenyl)benzene were synthesized according to published methods.[12,13] All reactions were handled under an inert atmosphere of nitrogen, while using proper Schlenk line techniques. A typical synthesis involved the following steps. First, a 100 ml Schlenk flask was charged with 40 mg of 3,3'-diaminobenzidine (0.19 mmol), 1.71 ml of 0.22 M HCl (0.38 mmol), and 30 ml of anhydrous DMF. The solution was cooled to -30 °C and a solution of 48.5 mg of 1,3,5-(3-formylphenyl)-benzene (0.13 mmol) in 25 ml of anhydrous DMR was subsequently added dropwise to the first solution. The temperature was maintained at -30 °C until an yellowish brown solution was formed. The reaction was allowed to cool to ambient temperature and left to stir under nitrogen overnight. The flask containing the reaction mixture was flushed with air for 15 minutes and capped tightly. The reaction mixture was heated in an oven at 130 °C at a ramp rate of 0.5 °C/min for 3 days. The resulting yellowish brown product was isolated via filtration over a medium glass frit and subsequently immersed in DMF (20 ml, 18 hrs) and then in acetone (3 x 20 ml, 18 hrs). The product was dried under vacuum at 120 °C and 1.0×10^{-5} Torr for 20 hrs to afford a pale yellow fluffy solid.

Nitrogen Uptake

Nitrogen uptake experiments were performed using a Quantachrome Autosorb IQ2 volumetric analyzer using adsorbates of UHP grade. The procedure was as follows: roughly 50 mg of sample was inserted into a 9 mm bulb and the sample was degassed at on the MasterPrep 120 °C and 150 mTorr for 12 h. The sample was subsequently degassed using the degassing station attached to the Autosorb under similar conditions. The bulb was backfilled with nitrogen and

the precise weight of the sample after activation was calculated. After returning the sample to the analyzer, the experiments were run at a controlled temperature of 77 K. Surface area, pore volume, and pore size distributions were calculated from the adsorption branch of nitrogen uptake isotherms using nonlocal density functional theory (NLDFT), assuming slit-like pores.

FT-IR Spectroscopy

Fourier transform infrared (FT-IR) spectra were collected to observe structures pre and post doping. A small amount of sample was placed directly onto a Smart ATR using a Nicolet Nexus 670 FTIR spectrometer and scanned from 4000 to 400 cm^{-1}, averaging 16 scans at a 1 cm^{-1} interval with a resolution of 4 cm^{-1}. Background scans were performed prior to loading each sample.

Raman Spectroscopy

Raman spectroscopy was performed using a Horiba LabRam 500 equipped with a ccd detector and an Nd/Yg source. Spectra were collected at an excitation wavelength of 532.11 nm, an acquisition time of 1 second frames for 30 frames per spectrum, and spectral range of 400-2200 cm^{-1}.

NMR Spectroscopy

MAS NMR experiments were performed on a 17.6 T (750 MHz) wide bore (Bruker, Billerica, MA) spectrometer using a Bruker BL3.2 HX 3.2 mm MAS probe (tuned to either ^1H-^{31}P or ^1H-

^{13}C) and a Bruker BL4 HXY 4 mm MAS probe (tuned to ^{1}H-^{13}C-^{15}N). Spinning was regulated at 10.0 kHz ± 5 Hz using a Bruker MAS II pneumatic MAS controller. All experiments were performed with a variable temperature set to 25 °C with a Bruker BVT-3000 temperature controller. ^{13}C experiments employed ramped cross polarization [Metz G. Wu X.L. Smith S.O. Ramped-Amplitude Cross Polarization in Magic-Angle-Spinning NMR] and SPINAL-64 ^{1}H decoupling [B.M. Fung, A.K. Khitrin, Konstantin Ermolaev, An Improved Broadband Decoupling Sequence for Liquid Crystals and Solids] during acquisition, with a nutation frequency of ~40 kHz. Recycle delays were 3 and 60 s for ^{1}H/^{13}C and ^{31}P spectra, respectively. Spectra were referenced to adamantine externally, assuming the downfield peak of 38.48 [Corey R Morcombe, Kurt W. Zilm, Chemical shift referencing in MAS solid state NMR]. NMR spectra were processed with X apodization and zero filled prior to Fourier transformation.

X-Ray Diffraction Measurements

Powder X-ray diffraction (XRD) experiments were performed using a a Panalytical X'pert pro multipurpose diffractometer (MPD) with Cu Kα radiation.

Scanning Electron Microscopy Images and Energy Dispersive Spectroscopy (EDS)

For scanning electron microscopy (SEM), imaging samples were prepared by dispersing the material onto a sticky carbon surface attached to a flat aluminum sample holder. The samples were then coated with platinum at 1×10^{-4} mbar of pressure in a nitrogen atmosphere for 120 s before imaging. Images were taken on a Hitachi SU-70 Scanning Electron Microscope.

Energy dispersive X-ray spectroscopy (EDX) and EDS were used for elemental analysis/ chemical characterization and elemental mapping of doped and undoped samples. Experiments were performed with accelerating voltage of 15 kV.

Acid-base Titration Experiments

Sample preparation included immersing the polymer in a specific concentration of phosphoric acid (either 3M or 85 wt%). The sample was left to stir at 40 °C overnight. The sample was subsequently filtered and dried. Upon drying, the sample was transferred to 50 ml of DI water and left to stir overnight at 40 °C. The filtrate was collected and used in the titration experiments. Titrations were carried out under ambient conditions using a **** pH meter. Additions of potassium hydroxide were made using an air displacement micropipette and the measured pH was allowed to equilibrate between additions.

Thermogravimetric Analysis (TGA) Experiments

Thermogravimetric analysis was carried out using a TA Instruments Q-5000IR series thermal gravimetric analyzer with samples held in 50 μL platinum pans under an atmosphere of nitrogen with a flow rate of 25.0 ml/min (heating rate 10 °C/min). Samples masses ranged from less than 1 mg to 15 mg.

Acid Doping Procedure and Pelletization

Samples were immersed in specific concentrations of phosphoric acid (~50 ml) and were left to stir at 40 °C overnight. The doped material was filtered and left to dry under vacuum filtration conditions. Once dried, the material was pressed into a uniform pellet (13 mm diameter) of varying thickness using a 13 mm IR dye set and a hydraulic press.

Electrochemical Impedance Spectroscopy (EIS)

Sample preparation included adhering carbon or copper tape (conductive adheasive) to the pelletized sample (see previous section). The sample was then cured for 2 hours at 40 °C. Subsequently, the electrodes were connected to the ends of the copper/carbon tape. Final measurements were taken using a more practical setup. The pellets were placed inside a Electrochem proton exchange membrane fuel cell, model FC-05-02, that was equipped with a gold plated current collector, graphite separator plate with a serpentine flow pattern, and silicon rubber heaters that were controlled using a temperature regulating apparatus. Proton conductivity studies were carried out via the 2-probe method, using a CH Instruments 760e potentiostat in the range of 0.1 Hz – 100 KHz, amplitude of 0.1 Volts, and 10 points/decade.

2.3 Results and Discussion

2.3.1 Synthesis of BILP-16 (AC) and Characterization

The goal of this project was to investigate the feasibility of using intrinsically porous benzimidazole-based materials for use as PEMs. A representative material, BILP-16 (AC), was chosen from this class of polymers and was synthesized using a previously published

procedure.[13] The overall reaction scheme, with a proposed mechanism for the formation of the

benzimidazole moiety, is shown in Figure 2.1 and Figure 2.2, respectively.[13]
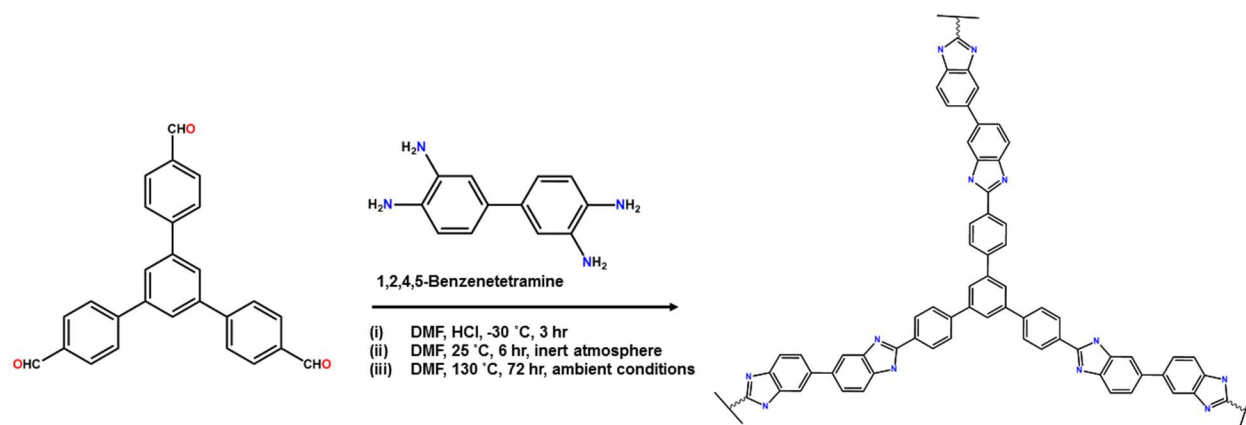
Figure 2.1 Synthetic procedure for the formation of BILP-16 (AC).[1]
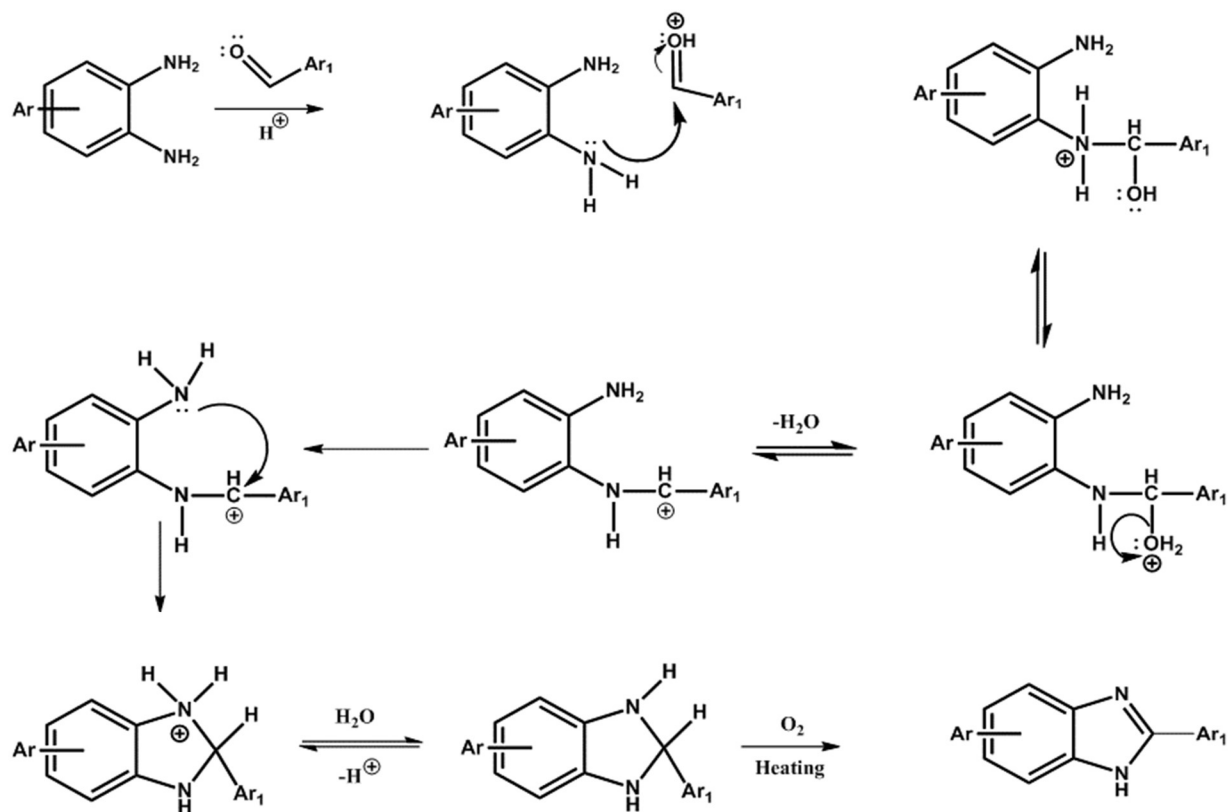
Figure 2.2 Proposed mechanism of imidazole moiety via catalytic acid process.[13]

Protonation occurs at the carbonyl, followed by nucleophilic attack at the electropositive benzylic carbon of the aldehyde. Proton migration to the more electronegative oxygen atom occurs, followed by the loss of water, which creates an extremely reactive carbocation species. The electrophilic carbocation is subsequently attacked by the adjacent amine, creating a ring closure step. The loss of a proton on the electropositive nitrogen regenerates the catalyst and the benzimidazole moiety is created upon heating in the presence of oxygen.

Successful synthesis of BILP-16 (AC) was confirmed via a multitude of characterization techniques. Surface area was determined from multilayer physisorb adsorption analysis and evaluation of the resulting nitrogen isotherms. Analysis revealed a hybrid type II/IV isotherm and pore size distribution indicates a microporous material, with the bulk of pores having pore sizes under 1 nm. Analysis of the adsorption branch gave a surface area of 649 m^2g^{-1}.

Analysis of infrared spectra for the starting materials and the final product against previously published spectra indicated successful synthesis of BILP-16 (AC). The disappearance of the two bands at 3346 cm^{-1} and 3491 cm^{-1}, corresponding to symmetric and asymmetric primary amine stretches, indicate the consumption of 3,3'-diaminobenzidine. The absence of the carbonyl stretch centered at 1684 cm^{-1} indicates the consumption of 1,3,5-(4-formylphenyl)-benzene. This aldehyde band is shifted a lower frequency due the resonance of the benzaldehyde moiety and additional conjugation over the entire molecule. The peaks at 3425 cm^{-1} and 3220 cm^{-1} correspond to N-H stretching peaks of free N-H bonds and hydrogen bonded N-H band, respectively.[1] Additionally, the emergence of the peak centered at 1620 cm^{-1} (C=N) indicates the formation of the imidazole ring.[13]

The sample was further characterized by solid state ^{13}C NMR and the resulting spectrum was analyzed and cross-referenced with previously published data.[13] The peak centered at 152 ppm is characteristic of a benzimidazole moiety and corresponds to the carbon donated by the aldehyde building block.[13] Powder XRD analysis gave a featureless spectrum, indicative of an amorphous material and scanning electron microscopy images confirmed the material's amorphic nature.

Aggregates of an oblong spherical morphology were observed and EDS elemental mapping showed even distribution of carbon and nitrogen.

After considerable analysis of the material, it was concluded that BILP-16 (AC) was successfully synthesized. It was also the aim of this project to investigate the proton conduction behavior of BILP-16 (AC). It was the desire of this research team to test the feasibility of this material for use as an acid-doped proton exchange membrane in fuel cell applications.

2.3.2 Acid Doping

After successfully synthesizing the polymer, the effect of acid doping was studied. It was desirable to understand the effect phosphoric acid (PA) loading had on morphology, mechanical, chemical, and thermal stability, and most importantly, proton conduction behavior. A simple illustration of the doping procedure is shown in Figure 2.3.
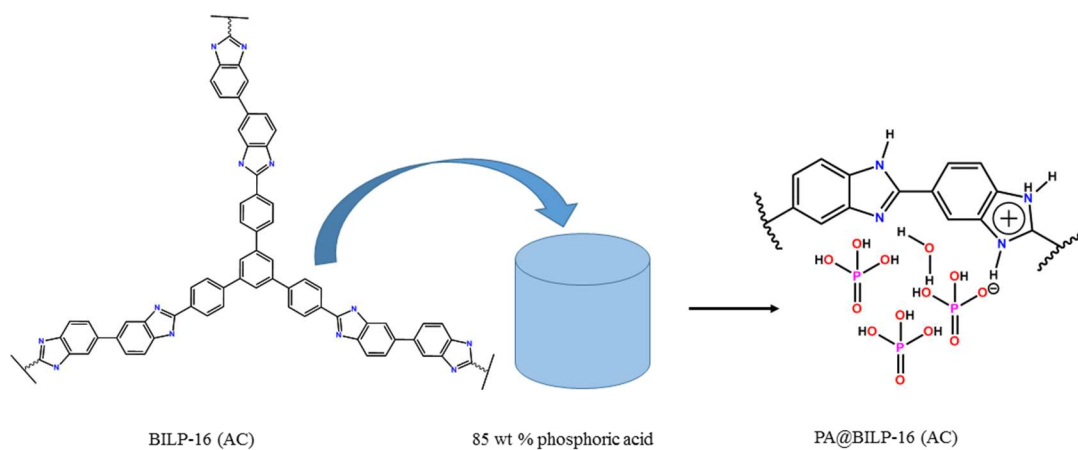
Figure 2.3 Illustration of the doping procedure for PA@BILP-16 (AC).

After immersion in 85 weight percent phosphoric acid for 24 hours at 40 °C, acid doping of

BILP-16 (AC) was validated by analysis of nitrogen adsorption isotherms. Prior to analysis, the

first indication of doping was seen by the color and texture change of the material. The material

changed from a light brown to a dark brown and from a fluffy powder to chalky substance, pre

and post doping, respectively. Adsorption spectra showed that the polymer retained its

microporous nature after doping, but there is a substantial drop in surface area from 649 m^2g^{-1} to

145 m^2g^{-1} for the pristine sample and the phosphoric imbedded material, respectively (Figure

2.4). It is worth mentioning that this data was collected on a sample that was doped with 3M

phosphoric acid and that surface area was shown to drop even more significantly upon

saturation.
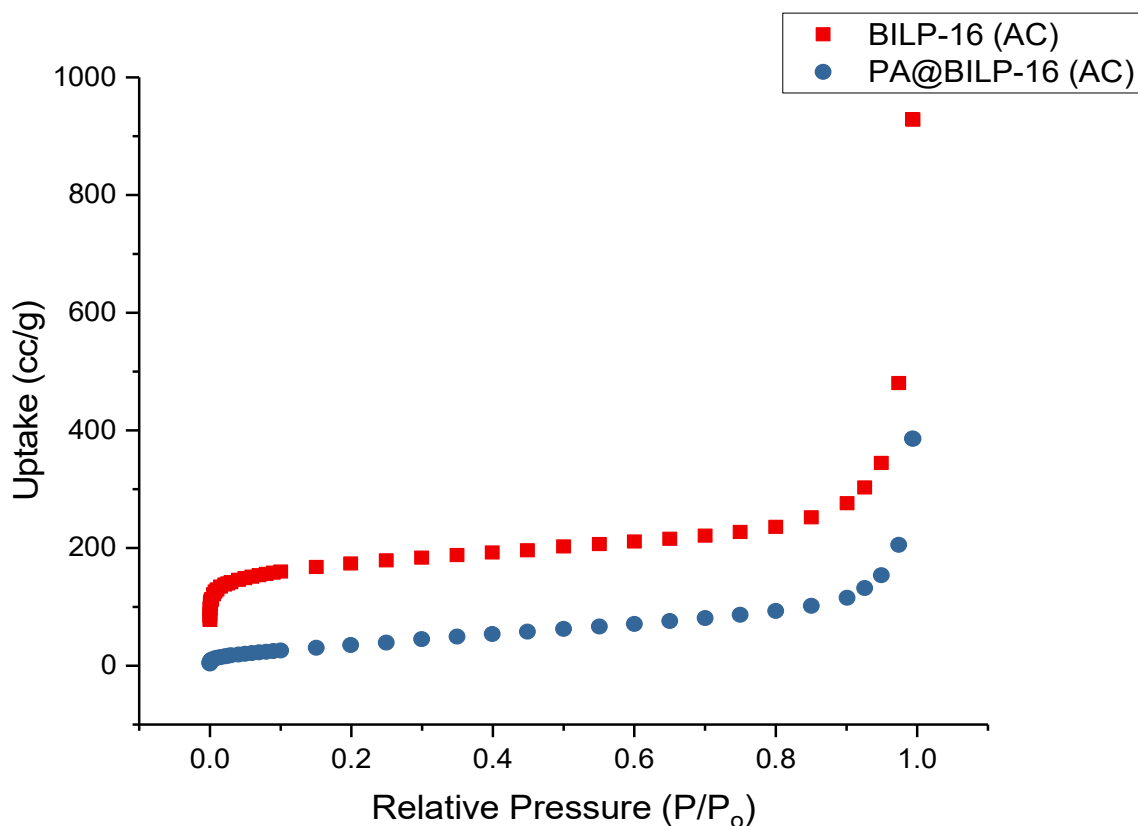
Figure 2.4 Nitrogen uptake isotherms for BILP-16 (AC) (red squares) and PA@BILP-16 (AC) (blue circles).

^{31}P NMR spectra indicate the presence of phosphoric acid within the polymer matrix (Figure 2.8) SEM images seemed to reveal a change in morphology, but upon closer investigation, the spherical morphology is retained. It is interconnected by phosphoric acid that resides on the surface and that is interwoven within the network. This binding of aggregates can explain the transformation of the material to a putty-like material, post-doping.
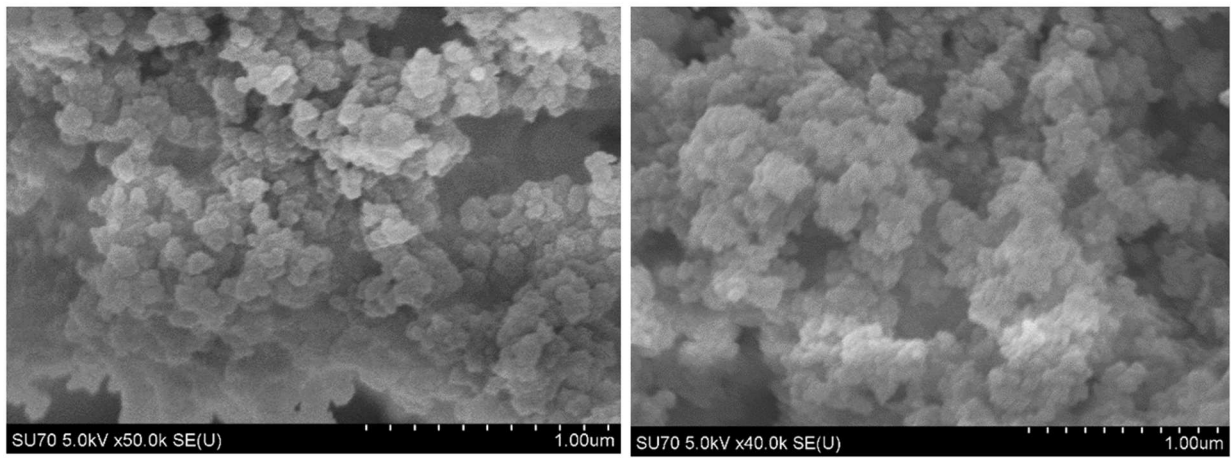
Figure 2.5 SEM images of BILP-16 (AC)
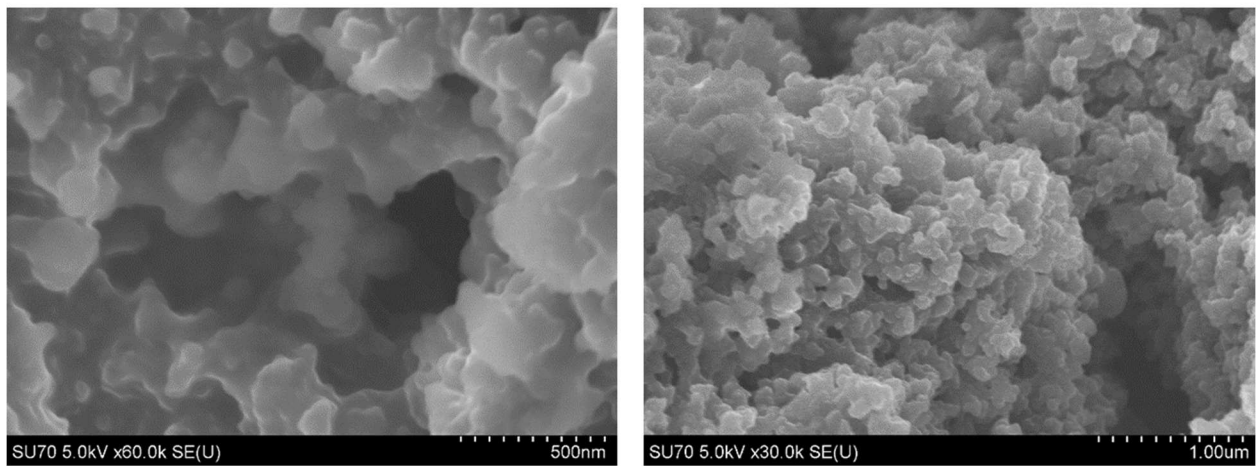
Figure 2.6 SEM images of PA@BILP-16 (AC)

^{13}C NMR was performed on both the pristine and doped polymer and is shown in Figure 2.7.
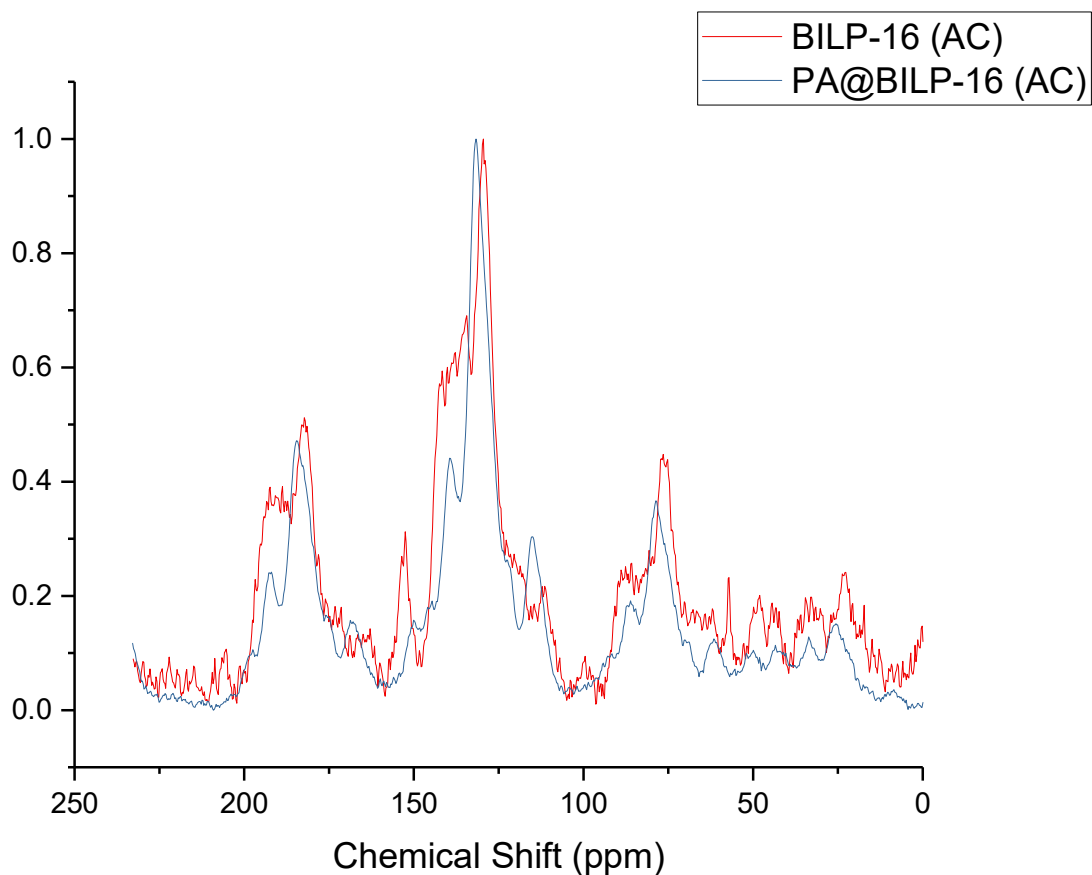
Figure 2.7 ^{13}C NMR spectra overlay of BILP-16 (AC) (red) and PA@BILP-16 (AC) (blue).

Peak assignments were aided by previously published data. ^{13}C NMR confirms that there is no structural damage to the polymer upon doping, with only slight shifts downfield of most peaks due to de-shielding caused by the introduction of phosphoric acid into the matrix.

2.3.3 Phosphate Species

Investigation into the doping behavior of these three-dimensional benzimidazole-based porous polymers was conducted using solid state ^{31}P and ^{1}H NMR. Figure 2.8 shows a very intense peak at 0.24 ppm for PA@BILP-16 (AC), with no peaks in the pristine sample. The peak observed in the doped sample corresponds to free H_3PO_4.
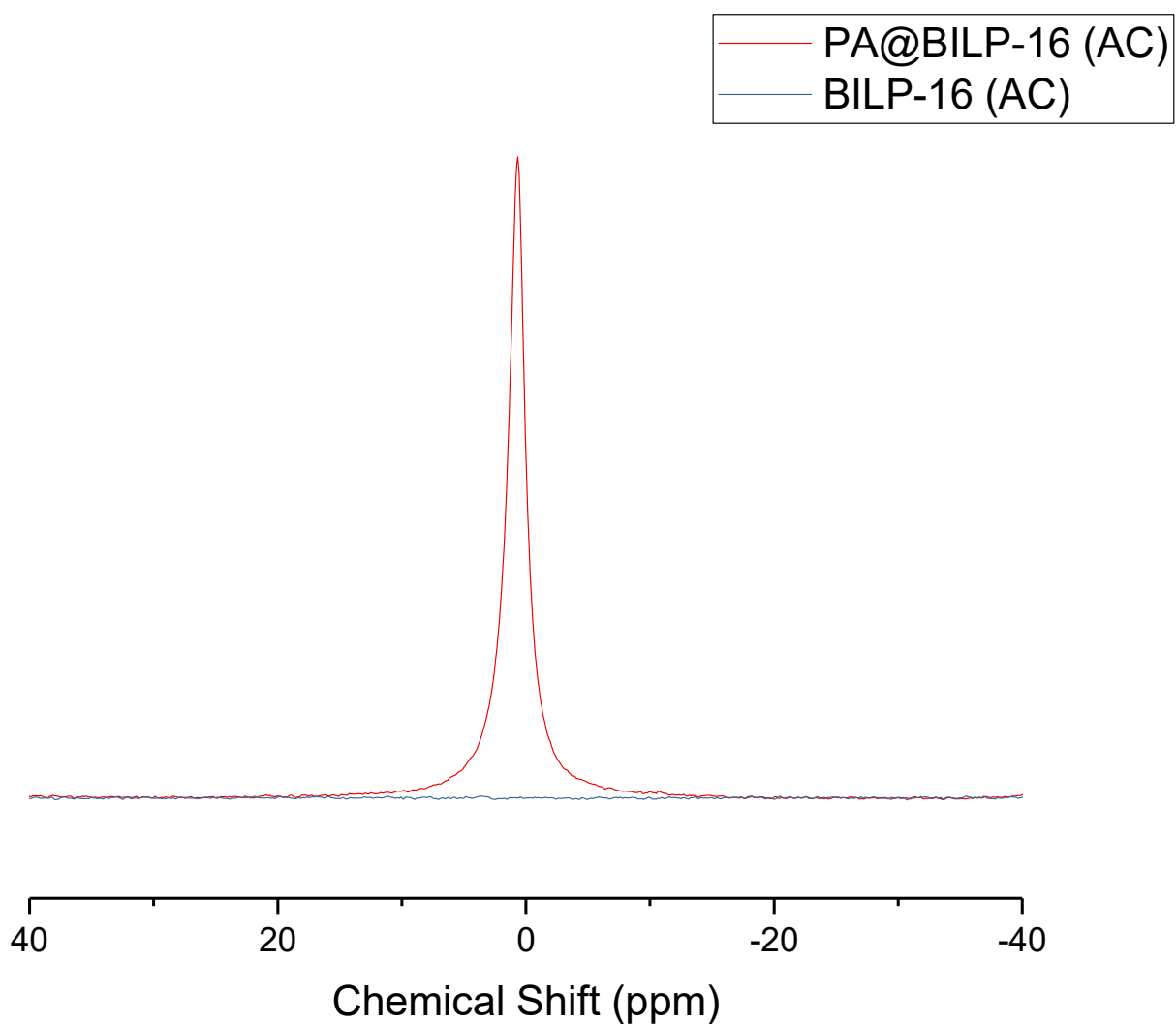
Figure 2.8 ^{31}P NMR spectra overlay of BILP-16 (AC) and PA@BILP-16 (AC).

Interestingly, there were no other peaks observed and this would lead one to believe that there is no "bonded acid" in the system, but the appearance of a weak intensity broad peak at 2758 cm-1 in the FT-IR spectrum (Figure 2.9) of PA@BILP- 16 (AC) is indicative of protonation. In addition, Figure 2.9 shows a medium peak at 1112 cm^{-1} corresponding to a vibrational peak for the $H_2PO_4^-$ species. The disappearance of the N-H stretching bands at 3400 cm^{-1} is characteristic of acid doping. Raman spectroscopy studies assisted in the understanding of doping behavior and can be seen in Figure 2.10. With the aid of work by Bouchet *et al.* and Rodolph, Table 2.1 was created and lists the FT-IR peaks for PA@BILP-16 (AC), along with peak assignments.[15,16] A very weak peak emerges in the Raman spectrum for PA@BILP-16 (AC) at 911 cm^{-1} that can be attributed to free phosphoric acid.[17] Additionally, blue shifts were observed for many characteristic peaks.
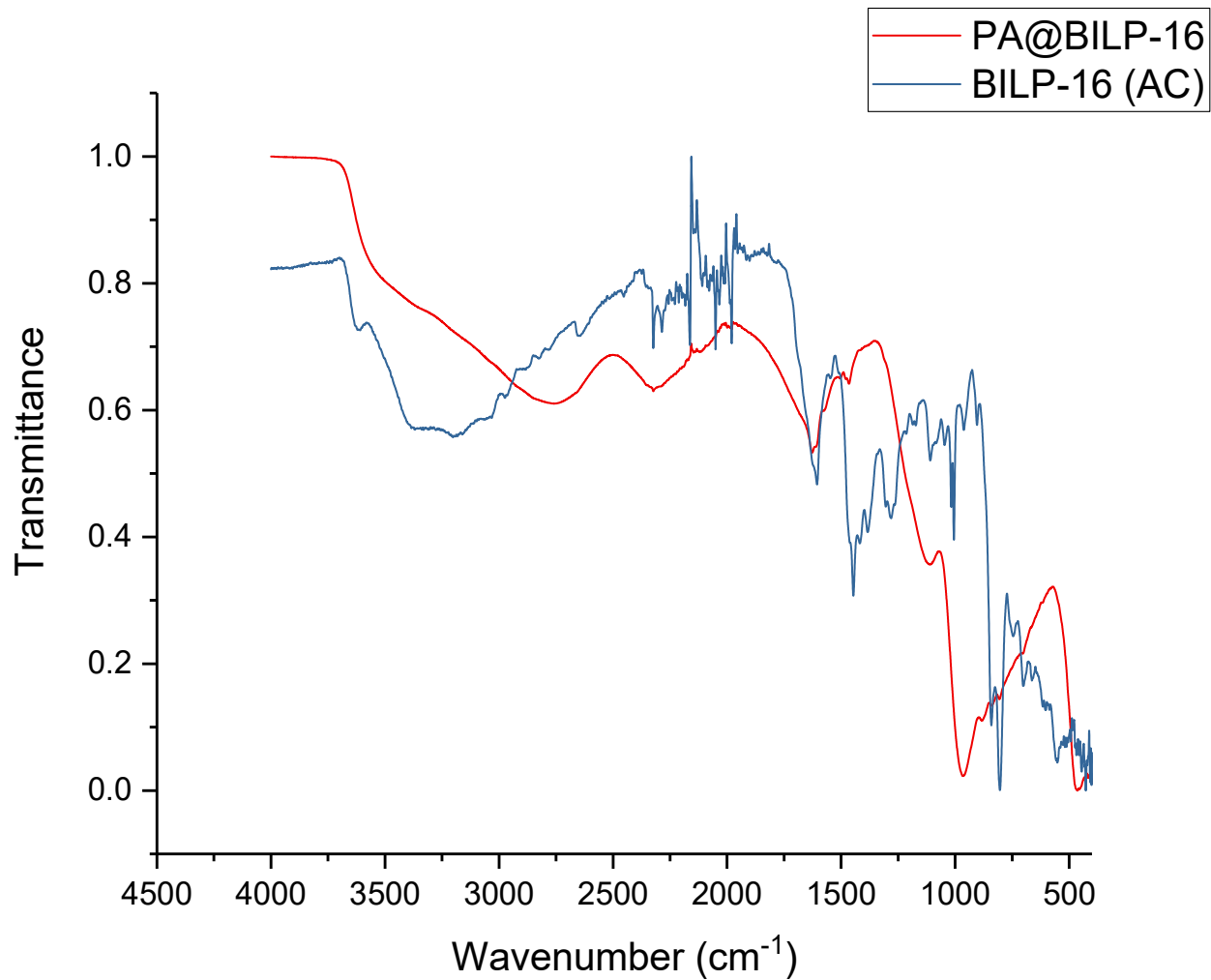
Figure 2.9 FT-IR spectra overlay of BILP-16 (AC) and PA@BILP-16 (AC).
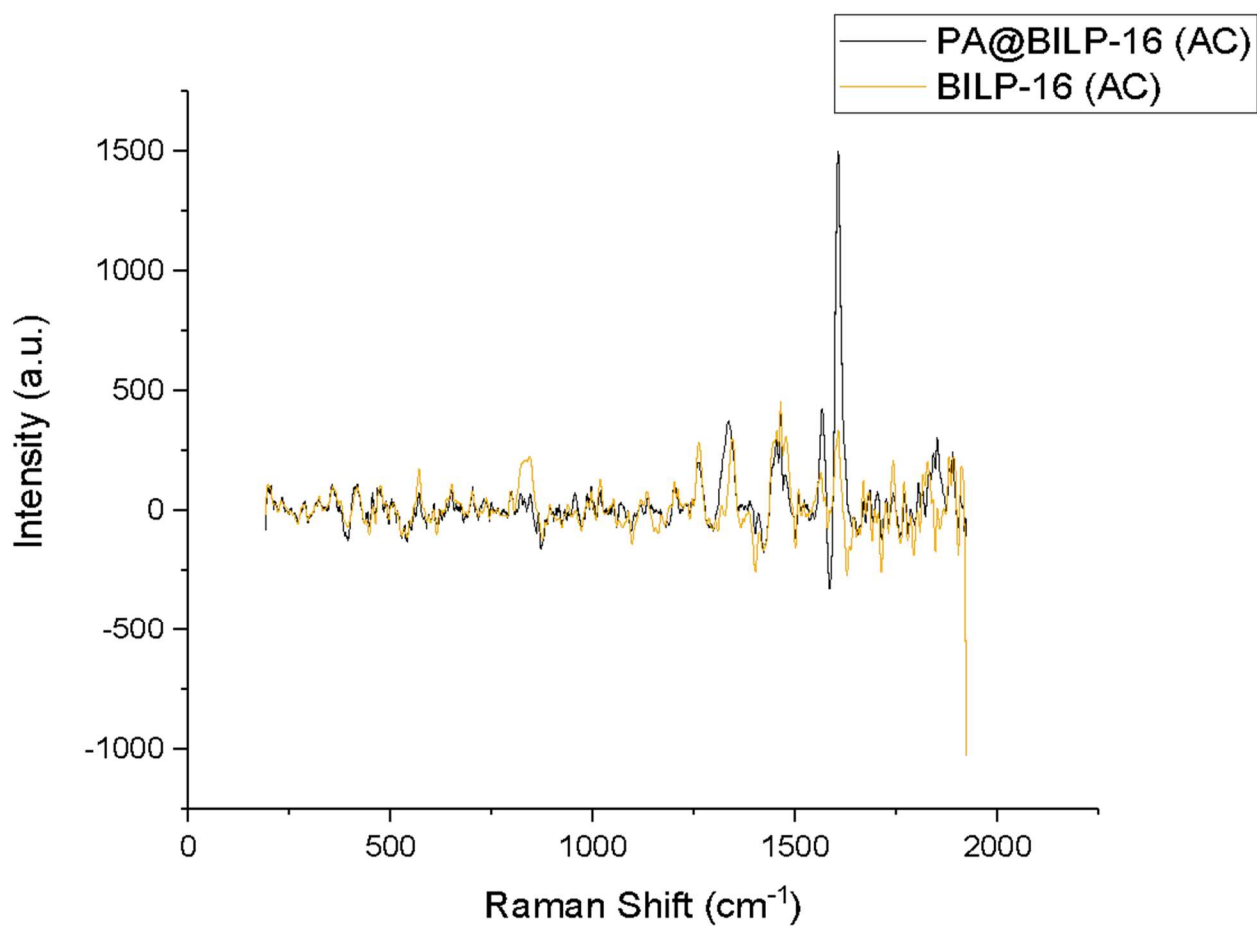
Figure 2.10 Raman spectral overlay of PA@BILP-16 (AC) (black) and BILP-16 (AC) (gold).

IR stretching bands (cm^{-1})	Assignment
468 (vS)	$\delta(PO_2)$ HPO$_4^{2-}$
878 (S)	$v_s(P(OH)_2)$ H$_2$PO$_4^-$
963 (vS)	$v(PO)$ H$_3$PO$_4$
1113 (m)	$v_s(PO_2)$ H$_2$PO$_4^-$

Table 2.1 FT-IR peak positions, as well as peak assignments for PA@BILP-16 (AC).

From the ^{1}H NMR spectrum of PA@BILP-16 (AC), one may also draw the same conclusion, with Figure 2.11 showing a single peak centered at 8 ppm for PA@BILP-16. Detailed proton NMR studies of phosphoric acid doped polybenzimidazole (PBI) indicated that in reality, this peak is a superposition of multiple peaks.[22] The broadening of these peaks can be attributed to slower exchange interactions between the polymer and the free acid caused by higher kinematic viscosity of the free phosphoric acid.[23-26]
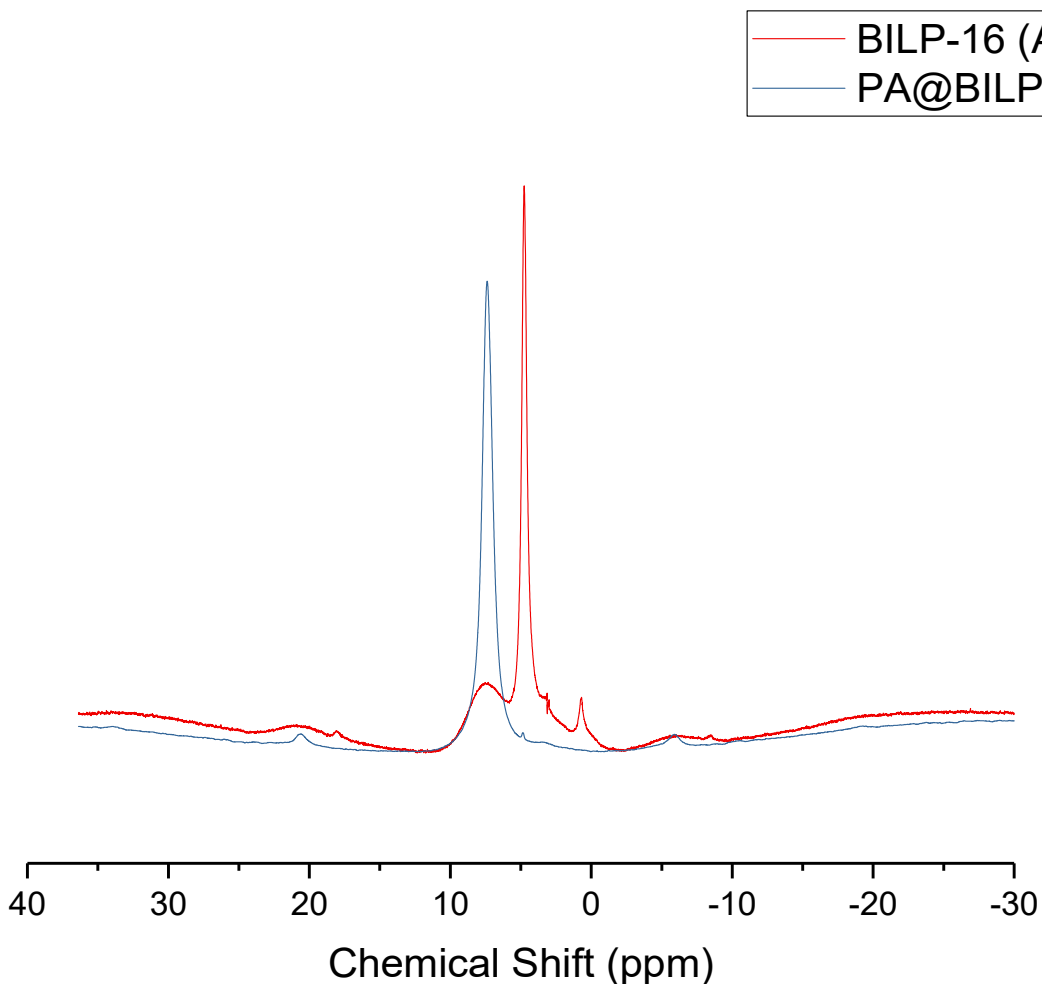
Figure 2.11 ^{1}H spectra overlay of BILP-16 (AC) and PA@BILP-16 (AC).

3.3.4 Proton Conduction

Quantification of Acid Doping

It has been well documented that proton conductivity is directly dependent upon acid content and this work set out to investigate the ability of the highly porous material to adsorb large amounts of phosphoric acid into its network. Doping behavior was investigated via simple titration experiments. After doping and drying, the material was immersed in 50 ml of deionized water at 40 ˚C and allowed to stir overnight. After filtering the polymer, the filtrate was collected and titrated with 0.1 M KOH. Figure 2.12 shows a titration curve for acid doping level determination.
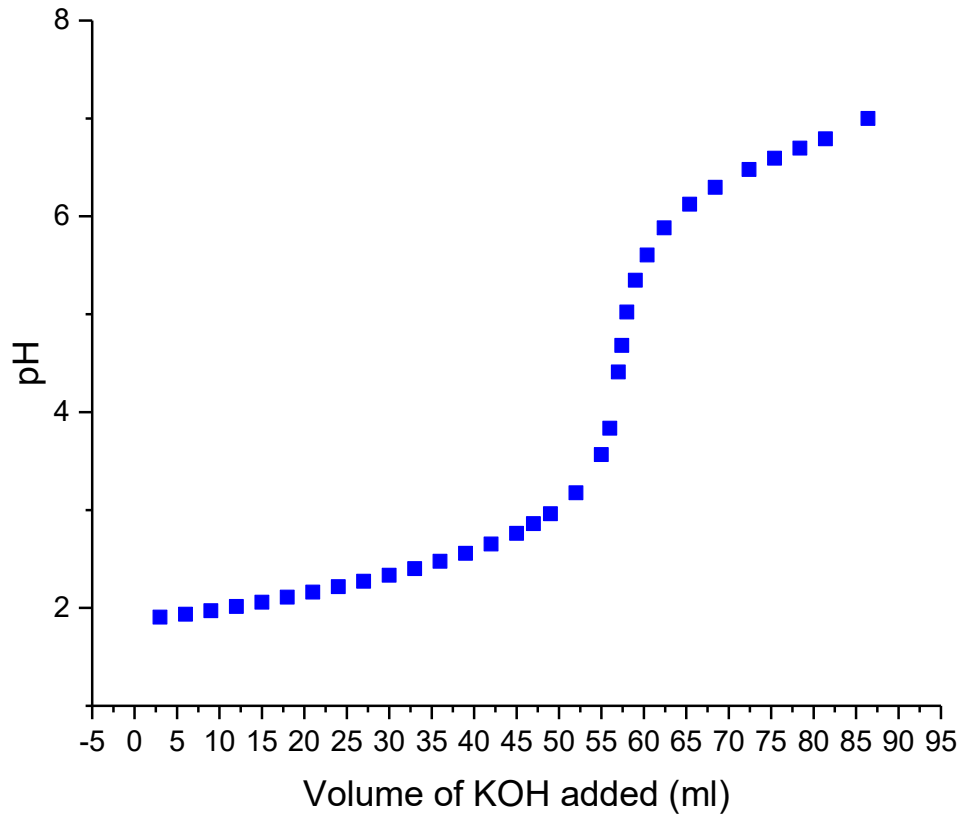
Figure 2.12 Acid-base titration of PA@BILP-16 (AC) with 0.1M KOH

The first equivalence point was determined and the acid content was calculated using Formula 1, where V_{KOH}, C_{KOH}, W_{dry}, and MW represent the volume of the titrant, in this case potassium hydroxide, the concentration of the titrant, the weight of the polymer after drying, and the molecular weight of one repeating unit of the polymer, respectively.

$$Acid\ doping\ level\ = \frac{(V_{KOH})(C_{KOH})}{\left(\frac{W_{dry}}{MW}\right)} \qquad (1)$$

The acid content is described as moles of acid per polymer repeating unit (PRU). It was found that BILP-16 (AC) was able to achieve an extremely high uptake of 56 moles of phosphoric acid per repeating unit of the polymer. Such a high uptake is attributed to high porosity, large pore volume, and high nitrogen content.

Additionally, the acid doping level can be calculated from the mass of the pristine polymer and the mass of the doped material using Formula 2,

$$Acid\ doping\ level = \frac{W_d}{W_i} \cdot \frac{M_{w-ALP6}}{M_{w-H3PO}} \tag{2}$$

Where W_d, W_i, M_{w-ALP6} and $M_{w-H3PO4}$ are the difference in masses between the doped and pristine material, the initial mass of the undoped polymer, the molecular weight of a single repeating unit of BILP-16 (AC), and the molecular weight of phosphoric acid, respectively.[18] It should be noted that these values take into account any adsorbed water. Further experiments can isolate the acid doping from the water doping. Taking into consideration the water doping, these values should correlate well with previously published data on linear PBI samples doped with phosphoric acid.[19]

Thermogravimetric analysis experiments were performed on the saturated sample and are shown in Figure 2.13. From figure 2.13 it was observed that there was an initial weight loss of 2.05 mg

(13.2 wt%) corresponding to the evaporation of water. A second weight loss was observed that corresponds to the dehydration/polymerization of phosphoric acid (4.29 mg, 27.56 wt%).
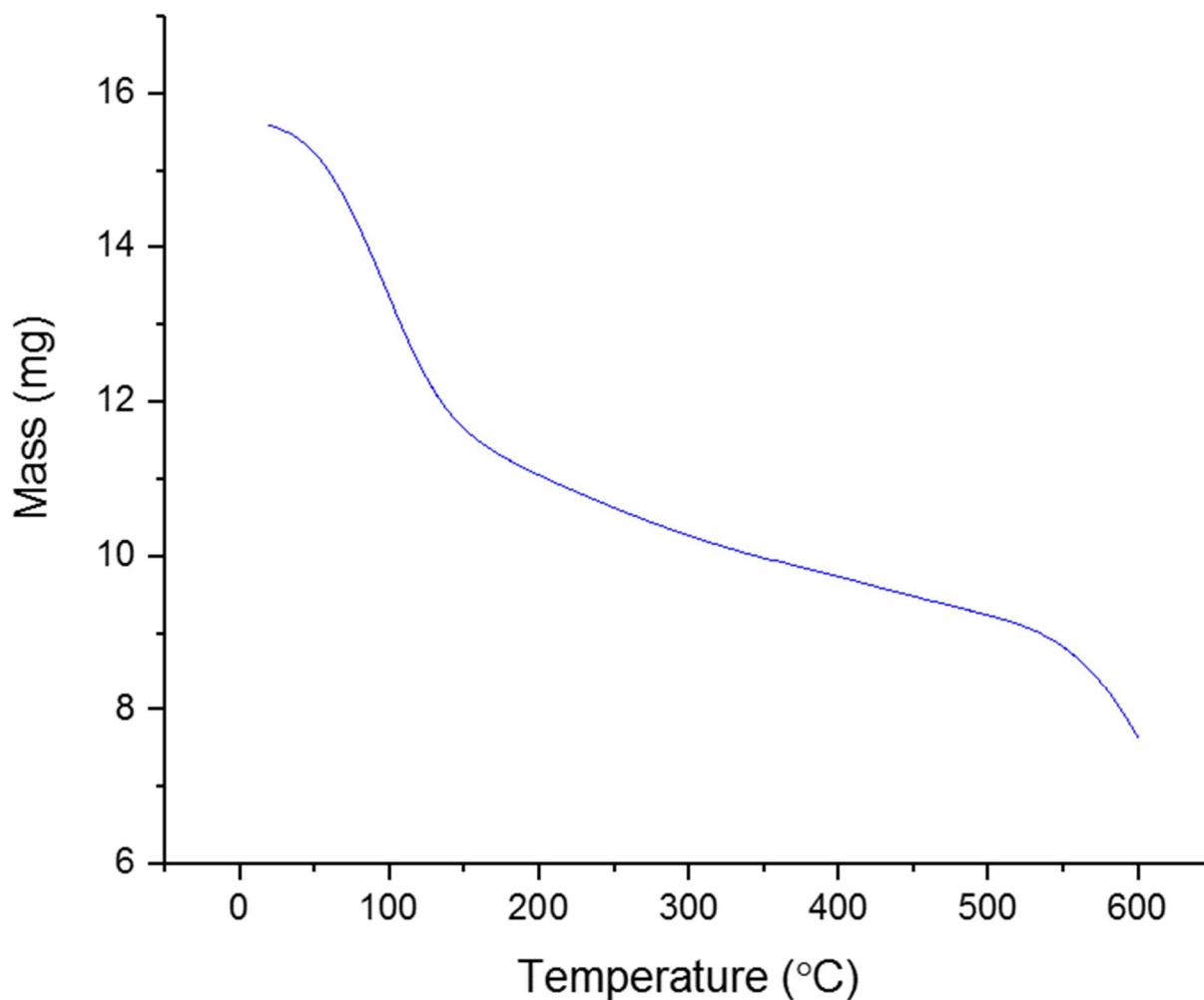
Figure 2.13 Thermogravimetric Analysis of PA@BILP-16 (AC)

These findings do not correlate well with previous findings using other techniques and it was determined that this is not an effective method for quantifying acid doping. This is due to the polymerization of phosphoric acid and the intercalation within the network of the polymer. The

polymerized acid does not evaporate, but instead, decomposes simultaneously with the original material.

Elemental mapping indicates even distribution of phosphoric acid within the porous network.
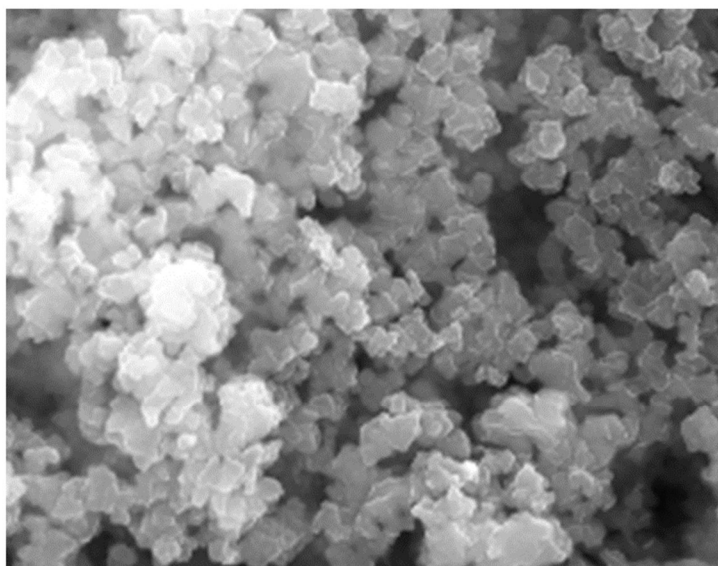
Figure 2.14 Cross sectional area of sample used for EDS.
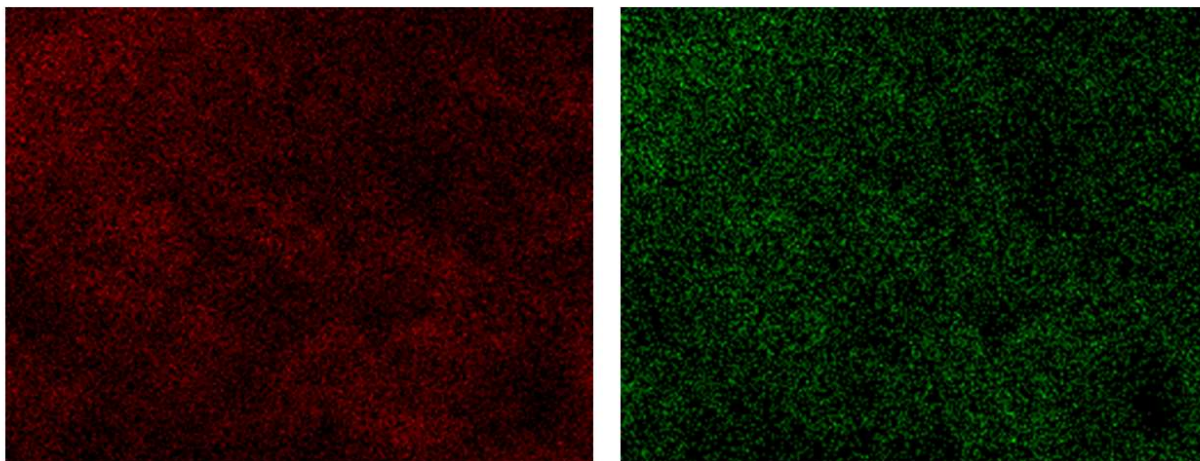
Figure 2.15 EDS elemental mapping of carbon atoms (red) and nitrogen atoms (green) in PA@BILP-16 (AC).
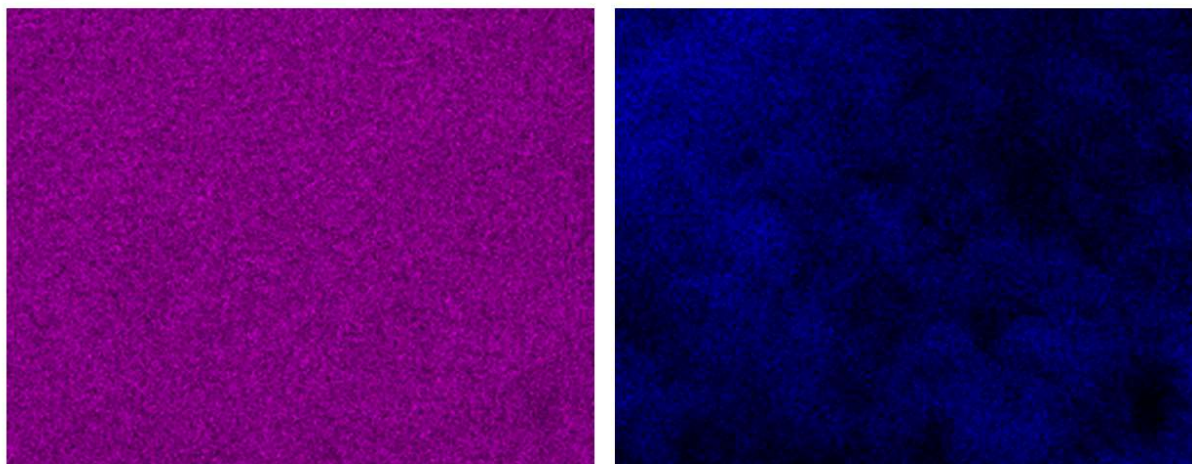
Figure 2.16 EDS elemental mapping of phosphorous atoms (pink) and oxygen atoms (blue) for PA@BILP-16 (AC).

Acid uptake was also studied using electron dispersive X-ray spectroscopy (EDX). Figure 2.17 shows the EDX spectrum of PA@BILP-16 (AC). The peak at 2.0 keV corresponds to a phosphorous peak and has an overwhelming area at ~ 38,000 counts versus a less intense peak centered at 0.27 keV for carbon of roughly only 650 counts. This, in conjunction with the titration experiments, indicate the polymer's ability to adsorb extremely high amounts of acid into its network.
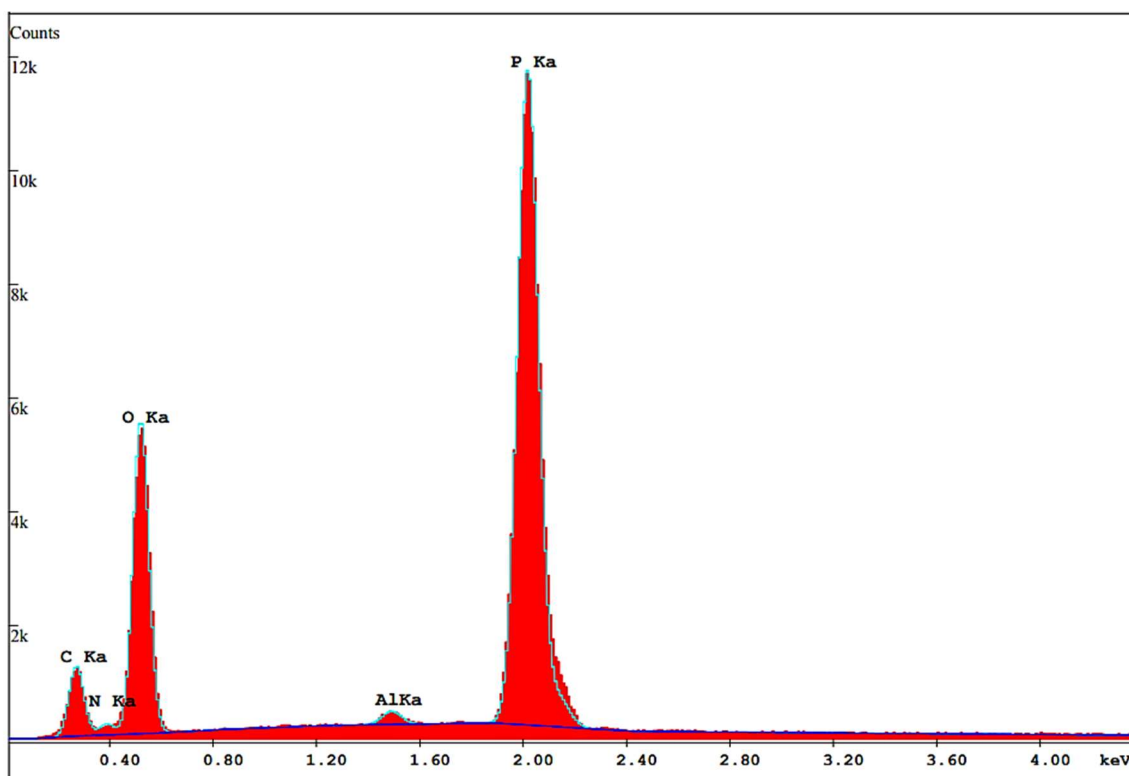
Figure 2.17 EDX spectrum of PA@BILP-16 (AC).

BILP-16 (AC) shows adequate chemical stability in acidic and basic conditions, with no observable degradation after immersion in 14 M H_3PO_4 and 4 M NaOH. SEM images (Figures 2.5 and 2.6) confirm the structural integrity of the polymer and indicate, in addition to the swelling

and weight gain due to the adsorption phosphoric acid, that the acid surrounds the exterior, interconnecting many localized aggregates and creating a chalk or putty like material, post doping.

Electrochemical Impedance Spectroscopy

Proton conductivity was measured by performing the well documented and widely accepted electrochemical impedance spectroscopic (EIS) experiments. The solid state electrolyte resistance was determined by evaluating the intercept with the real axis in the high frequency regime of the complex plane of a Nuyqist plot.[27] Figure 2.18 shows a Nyquist impedance plot for PA@BILP-16 (AC), where all conductivity measurements were performed at room temperature (298 K) and a relative humidity of zero (RH = 0%). Initial testing indicated that the pristine polymer was not conductive, but upon doping, achieved high values of proton conductivity. After equilibration, PA@BILP-16 (AC) produced a proton conductivity (σ) value of 2.50 x 10^{-2} S cm^{-1} at room temperature. This value was calculated using the following formula:

$$\sigma = \frac{L}{R \cdot A} \qquad (3)$$

where, σ, L, R, and A are the proton conductivity, membrane thickness, membrane resistance, and area of the membrane, respectively. Such a high value can be ascribed to the material's high surface area, relatively large pore volume, and high nitrogen content. Previous studies of the aliphatic analogue, PBI, by Cantero et al. showed a direct correlation between porosity and conductivity, with an increase in conductivity of a factor of ten from the bulk polymer to an initial porogen content of 70 wt %.[18]
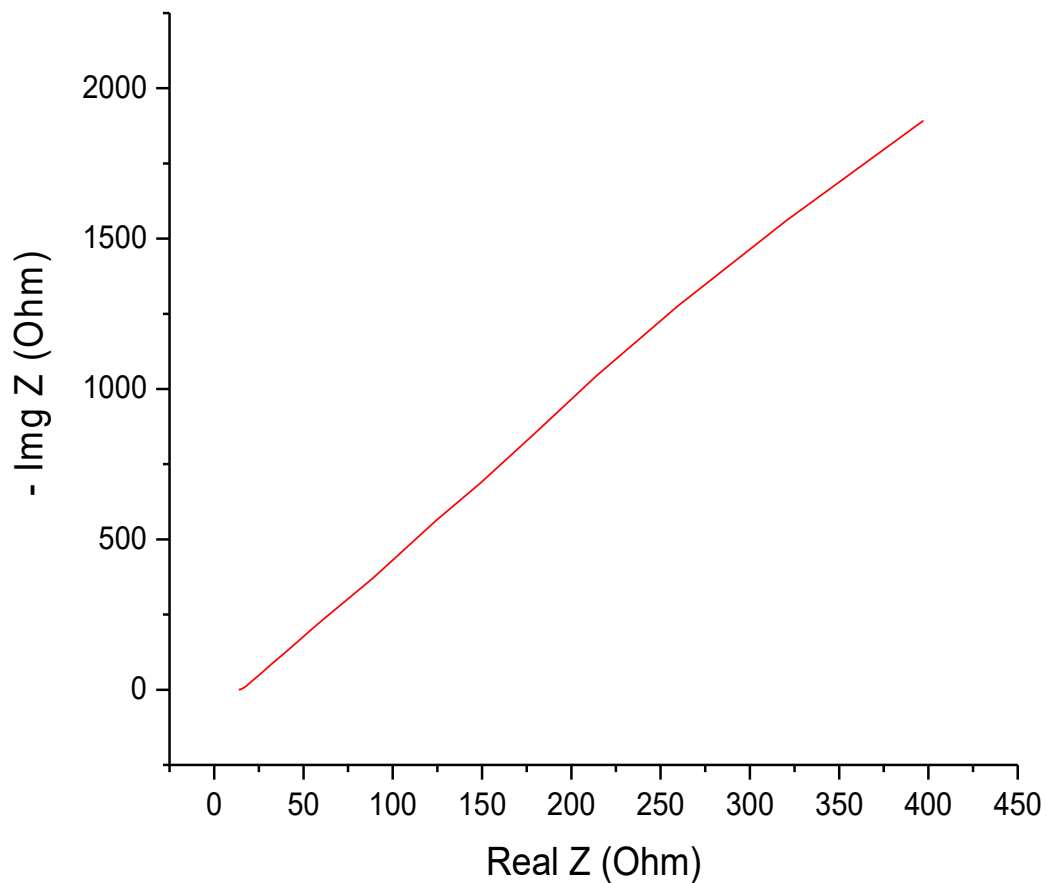
Figure 2.18 Nyquist impedance plot for PA@BILP-16 (AC) at room temperature.

Table 2.2 gives a representation of the best performing materials to date. It should be noted that most of these values were obtained at elevated temperatures and under highly hydrated conditions.

	Compound	Conductivity (Scm⁻¹)	Conditions	Reference
1	Nafion®	$\sim 1 \times 10^{-1}$	80°C, 98% RH	*J. Polym. Sci., Part B: Polym. Phys.* 2011, 49, 1437
2	H_3PO_4@BILP-16 (AC)	5.80×10^{-2}	60°C, 0% RH	*This Work*
3	H_3PO_4@PBI	5×10^{-2}	60°C, 0% RH	*Chem. Mater.*, 2005, 17, 21, 5329
4	SPEEK	2×10^{-2}	80°C, 98% RH	*J. Polym. Sci., Part B: Polym. Phys.* 2011, 49, 1437
5	H2SO4@MIL-101	6.0×10^{-2}	80°C, 20% RH	*J. Am. Chem. Soc.* 2012, 134, 15640
6	H_3PO_4@MIL-101	3×10^{-3}	150°C, 0.13%RH	*J. Am. Chem. Soc.* 2012, 134, 15640
7	PA@Tp-Azo	9.9×10^{-4}	25°C, 98% RH	*J. Am. Chem. Soc.* 2014, 136, 6570

Table 2.2 Top performing materials for use as proton exchange membranes (PEMs).

It has been well documented that temperature has a direct influence on fuel cell performance, including proton conduction within the membrane.[19] Figure 2.19 shows Nyquist plots for BILP-16 (AC) at varying temperatures.
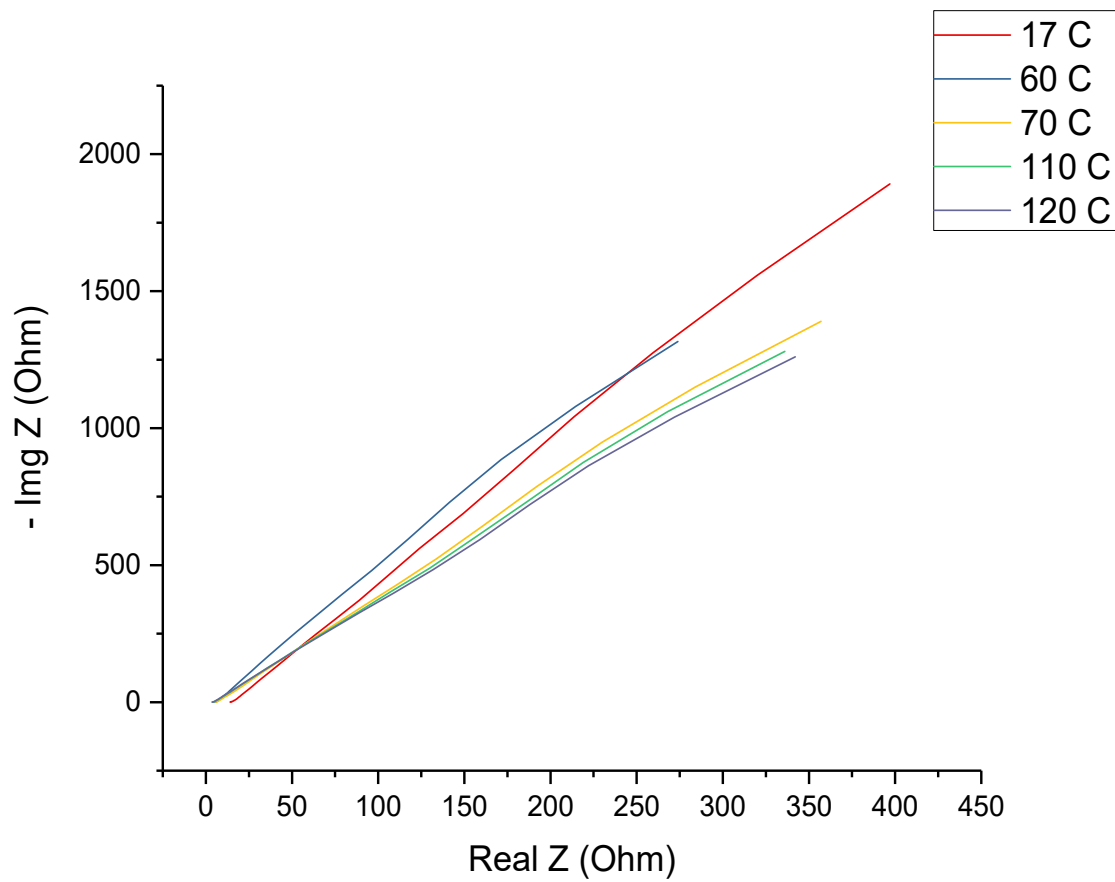
Figure 2.19 Nyquist impedance plots (overlay) of PA@BILP-16 (AC) at varying temperatures.

Materials similar to BILP-16 (AC) that exhibit a hoping-like proton conduction mechanism, the temperature dependent proton conductivity can be expressed by equation (4)

$$\sigma = \sigma_o^{\frac{E_a}{RT}} \qquad (4)$$

where σ is the proton conductivity, $σ_o$ is the pre-exponential factor, E_a is the activation energy, T is the temperature, and R is the ideal gas constant.[20]

This assumes that there is no change in concentrations along the temperature range studied. This is problematic due to the fact a loss in water was observed at temperatures above 60 °C. So, there is an increase in conductivity observed up to said temperature, followed by a decrease in conductivity caused by the loss of water. This drop in conductivity does occur infinitely, but instead, above 85 °C, an increase in conductivity was observed. This resulted from an increase in kinetics and can be explained using equation 3, but can be better explained using the Arrhenius plot of conductivity.

2.4 Conclusions

A novel material for use as a proton conductive membrane in proton electrolyte membrane fuel cells was synthesized. The pristine polymer showed limited signs of proton conductivity, but after doping with phosphoric acid, a high proton conductivity value of 5.8×10^{-2} S cm^{-1} was achieved at 60 °C under anhydrous conditions. Such a high value was possible due to the high porosity, relatively large pore volume, and high nitrogen content that allowed for saturated acid doping values exceeding 56 moles PRU. The material adsorbed over ****wt % through anchoring of H_3PO_4 to open nitrogen sites ("bonded acid") and free acid non-covalently trapped inside the pores of the matrix. Thermogravemetric analysis revealed a thermal stability exceeding 400 ˚C, while PA@BILP-16 (AC) mainted its adequate chemical stability in acid and basic media. It has been shown that nitrogen-rich porous organic frameworks doped with acid

possess many of the desired features for use as polymer electrolyte membranes in PEMFCs. More detailed research into structure-property relationships of nitrogen-rich porous organic frameworks under *in-situ* conditons using the recently acquired single and multi-stack fuel cell test stations will shed more light on the viability of these materials reaching commercialization.

Chapter 2 References

1. Herm, Z.R.; Bloch, E.D.; Long, J.R. *Chem. Mater.* **2014**, *26*, 323.

2. Sumida, K.; Rogow, D.L.; Mason, J.A.; McDonald, T.M.; Bloch, E.D.; Herm, Z.R.; Bae, T.H.; Long, J.R. *Chem. Rev.* **2012**, *112*, 724.

3. Li, Y.W.; Xu, J.; Li, D.C.; Dou, J.M.; Yan, H.; Hu, T.L.; Bu, X.H. *Chem. Commun.* **2015**, *51*, 14211.

4. Farrusseng, D.; Aguado, S.; Pinel, C.; *Angew Chem. Int. Ed.* **2009**, *48*, 7502.

5. Corma, A.; Garcia, H.; Xamena, F. *Chem. Rev.* **2010**, *110*, 4606.

6. Fang, Z.L.; Bueken, B.; De Vos, D.E.; Fischer, R.A. *Angew. Chem. Int. Ed.* **2015**, *54*, 7234.

7. Wang, H.; Su, J.; Zhang, D.S.; Chen, Q.; Wen, R.M.; Chang, Z.; Bu, X.H.; *Angew. Chem. Int. Ed.* **2015**, *54*, 5966.

8. Jia, Y.Y.; Zhang, Y.H.; Xu, J.; Feng, R.; Zhang, M.S.; Bu, X.H. *Chem. Commun.* **2015**, *51*, 17439.

9. Chandra, S.; Kundu, T.; Dev, K.; Addicoat, M.; Heine, T.; Banerjee, R. *Chem. Mater.* **2016**, *28*, 1489-1494.

10. Chandra, S.; Kundu, T.; Kandambeth, S.; BabaRao, R.; Marathe, Y.; Kunjir, S.M.; Banerjee, R. *J. Am. Chem. Soc.* **2014**, *136*, 6570-6573.

11. Mecerreves, D.; Grande, H.; Miguel, O.; Ochoteco, E.; Marcilla, R.; Cantero, I. *Chem. Mater.* **2004**, *16*, 604-607.

12. Rabbani, M.G.; El-Kaderi, H.M. *Chemistry of Materials*. **2011**, *23*, 1650-1653.

13. Altarawneh, S.; Islamoglu, T.; Sekizkardes, A.K.; El-Kaderi, H.M. *Environ. Sci. Technol.* **2015**, *49*, 4715-4723.

14. Rabbani, M.G.; El-Kaderi, H.M. *Chemistry of Materials*. **2011**, *23*, 1650-1653.

15. Bouchet, R.; Siebert, E. *Solid State Ionics.* **1999**, *118*, 287–299.

16. Conti, F.; Majerus, A.; Noto, V. D.; Korte, C.; Lehnert, W.; Stolten, D. *Physical Chemistry Chemical Physics.* **2012**, *14*, 10022-10026.

17. Rudolph, W. W. *Dalton Transactions.* **2010**, *39* (40), 9642–9653.

18. Mecerreyes, D.; Grande, H.; Miguel, O.; Ochoteco, E.; Marcilla, R.; and Cantero, I. *Chem. Mater.* **2004**, *16*, 604-607.

19. Wang, J.-T.; Wainright, J.; Savinell, R.F.; Litt, M. *J. Appl. Electrochem*. **1996**, 26, 7513.

20. Bruce, P. G. *Solid state electrochemistry*; Cambridge Univ. Press: Cambridge, 1995.

21. Schechter,A.; Savinell, R.F. *Solid State Ionics*. **2002**, *147*, 181–187.

22. Schechter, A.; Savinell, R.F.; Wainright, J.S.; Ray, D. *Journal of The Electrochemical Society*. **2009**, *156,* B283-B290.

23. J. R. P. Jayakody, S. H. Chung, L. Durantino, H. Zhang, L. Xiao, B. C. Benicewicz, and S. G. Greenbaum, J. Electrochem. Soc., *154*, B242 2007.

24. Shinde, D.B.; Aiyappa, H.B.; Bhadra, M.; Biswal, B.P.; Wadge, P.; Kandambeth, S.; Garai, B.; Kundu, T.; Durungot, S.; Banerjee, R. *J. Mater. Chem. A*. **2016**, *4*, 2682-2690.

Chapter 3

Azo-Linked Polymer-Based Proton Exchange Membranes

3.1 Introduction

Azo-linked polymers are another new class of polymers that, due to their chemical and physical properties, show promise in the field of proton exchange membranes. These materials exhibit high surface area, high pore volume, high chemical and thermal stability, and high nitrogen content. These properties should contribute to extrinsic proton conduction upon doping with a mineral acid. The pioneering work by Banerjee *et al.* in 2014, the first example of the use of COFs as proton exchange membranes, inspired this project.[1] Although the material published by that group is crystalline, it was proposed the amorphic nature of the material described herein should not hinder proton conduction.

3.2 Experimental Procedures

Materials

All chemicals were purchased from commercial suppliers (Acros Organics, Sigma Aldrich, or Frontier Scientic) and used without further purication, unless otherwise noted. N,N,N0 ,N0 - Tetrakis(4-aminophenyl)-1,4-phenylenediamine (TAPPA) was purchased from Combi-Blocks.

Synthesis of Azo-linked Polymer 6 (ALP-6)

ALP-6 was synthesized according to a previously published procedure.[1] A typical experiment involved the following steps. 40 mg of CuBr (0.279 mmol) and 160 mg of pyridine (2.023 mmol) were added to 11ml of toluene. The mixture was briefly sonicated and subsequently stirred in open atmosphere at room temperature for 3 hrs. The resulting mixture was added to 11 ml of THF that contained 100 mg (0.212 mmol) of N,N,N',N' -tetrakis(4-aminophenyl)-1,4-phenylenediamine. The resulting mixture was stirred in open atmosphere at 25 °C for 24 hrs, at 60 °C for 12 hours, and at 80 °C for 12 hours. The resulting product was isolated via filtration using a medium glass frit and was subsequently washed with THF and water. The product was further washed with 2 M NaOH, water, ethanol, THF, and chloroform. The final product was dried at 120 °C under vacuum (150 mTorr) for 12 hours. The final product gave a purplish brown powder.

Nitrogen Uptake

Nitrogen uptake experiments were performed using a Quantachrome Autosorb IQ2 volumetric analyzer using adsorbates of UHP grade. The procedure was as follows: roughly 50 mg of sample was inserted into a 9 mm bulb and the sample was degassed at on the MasterPrep 120 °C and 150 mTorr for 12 h. The sample was subsequently degassed using the degassing station attached to the Autosorb under similar conditions. The bulb was backfilled with nitrogen and the precise weight of the sample after activation was calculated. After returning the sample to the analyzer, the experiments were run at a controlled temperature of 77 K. Surface area, pore

volume, and pore size distributions were calculated from the adsorption branch of nitrogen uptake isotherms using nonlocal density functional theory (NLDFT), assuming slit-like pores.

FT-IR Spectroscopy

Fourier transform infrared (FT-IR) spectra were collected to observe structures pre and post doping. A small amount of sample was placed directly onto a Smart ATR using a Nicolet Nexus 670 FTIR spectrometer and scanned from 4000 to 400 cm^{-1}, averaging 16 scans at a 1 cm^{-1} interval with a resolution of 4 cm^{-1}. Background scans were performed prior to loading each sample.

Raman Spectroscopy

Raman spectroscopy was performed using a Horiba LabRam 500 equipped with a ccd detector and an Nd/Yg source. Spectra were collected at an excitation wavelength of 532.11 nm, an acquisition time of 1 second frames for 30 frames per spectrum, and spectral range of 400-2200 cm^{-1}.

NMR Spectroscopy

MAS NMR experiments were performed on a 17.6 T (750 MHz) wide bore (Bruker, Billerica, MA) spectrometer using a Bruker BL3.2 HX 3.2 mm MAS probe (tuned to either ^{1}H-^{31}P or ^{1}H-^{13}C) and a Bruker BL4 HXY 4 mm MAS probe (tuned to ^{1}H-^{13}C-^{15}N). Spinning was regulated at 10.0 kHz ± 5 Hz using a Bruker MAS II pneumatic MAS controller. All experiments were

performed with a variable temperature set to 25 °C with a Bruker BVT-3000 temperature controller. ^{13}C experiments employed ramped cross polarization [Metz G. Wu X.L. Smith S.O. Ramped-Amplitude Cross Polarization in Magic-Angle-Spinning NMR] and SPINAL-64 ^{1}H decoupling [B.M. Fung, A.K. Khitrin, Konstantin Ermolaev, An Improved Broadband Decoupling Sequence for Liquid Crystals and Solids] during acquisition, with a nutation frequency of ~40 kHz. Recycle delays were 3 and 60 s for ^{1}H/^{13}C and ^{31}P spectra, respectively. Spectra were referenced to adamantine externally, assuming the downfield peak of 38.48 [Corey R Morcombe, Kurt W. Zilm, Chemical shift referencing in MAS solid state NMR]. NMR spectra were processed with X apodization and zero filled prior to Fourier transformation.

X-Ray Diffraction Measurements

Powder X-ray diffraction (XRD) experiments were performed using a a Panalytical X'pert pro multipurpose diffractometer (MPD) with Cu Kα radiation.

Scanning Electron Microscopy Images and Energy Dispersive Spectroscopy (EDS)

For scanning electron microscopy (SEM), imaging samples were prepared by dispersing the material onto a sticky carbon surface attached to a flat aluminum sample holder. The samples were then coated with platinum at 1×10^{-4} mbar of pressure in a nitrogen atmosphere for 120 s before imaging. Images were taken on a Hitachi SU-70 Scanning Electron Microscope.

Energy dispersive X-ray spectroscopy (EDX) and EDS were used for elemental analysis/ chemical characterization and elemental mapping of doped and undoped samples. Experiments were performed with accelerating voltage of 15 kV.

Acid-base Titration Experiments

Sample preparation included immersing the polymer in a specific concentration of phosphoric acid (either 3M or 85 wt%). The sample was left to stir at 40 °C overnight. The sample was subsequently filtered and dried. Upon drying, the sample was transferred to 50 ml of DI water and left to stir overnight at 40 °C. The filtrate was collected and used in the titration experiments. Titrations were carried out under ambient conditions using a **** pH meter. Additions of potassium hydroxide were made using an air displacement micropipette and the measured pH was allowed to equilibrate between additions.

Thermogravimetric Analysis (TGA) Experiments

Thermogravimetric analysis was carried out using a TA Instruments Q-5000IR series thermal gravimetric analyzer with samples held in 50 μL platinum pans under an atmosphere of nitrogen with a flow rate of 25.0 ml/min (heating rate 10 °C/min). Samples masses ranged from less than 1 mg to 15 mg.

Acid Doping Procedure and Pelletization

Samples were immersed in specific concentrations of phosphoric acid (~50 ml) and were left to stir at 40 °C overnight. The doped material was filtered and left to dry under vacuum filtration conditions. Once dried, the material was pressed into a uniform pellet (13 mm diameter) of varying thickness using a 13 mm IR dye set and a hydraulic press.

Electrochemical Impedance Spectroscopy (EIS)

Sample preparation included adhering carbon or copper tape (conductive adheasive) to the pelletized sample (see previous section). The sample was then cured for 2 hours at 40 °C. Subsequently, the electrodes were connected to the ends of the copper/carbon tape. Final measurements were taken using a more practical setup. The pellets were placed inside a Electrochem proton exchange membrane fuel cell, model FC-05-02, that was equipped with a gold plated current collector, graphite separator plate with a serpentine flow pattern, and silicon rubber heaters that were controlled using a temperature regulating apparatus. Proton conductivity studies were carried out via the 2-probe method, using a CH Instruments 760e potentiostat in the range of 0.1 Hz – 100 KHz, amplitude of 0.1 Volts, and 10 points/decade.

3.3 Results and Discussion

3.3.1 Synthesis and Characterization

Azo-linked polymers used for this work were synthesized using a previously published procedure that employed an oxidative coupling reaction to polymerize aniline-like monomers.[1] The synthetic conditions can be found in Figure 3.1. The monomer was chosen due to its rigid

structure and high nitrogen content. Post polymerization, the product was washed and activated, and subsequently subjected to nitrogen uptake studies.
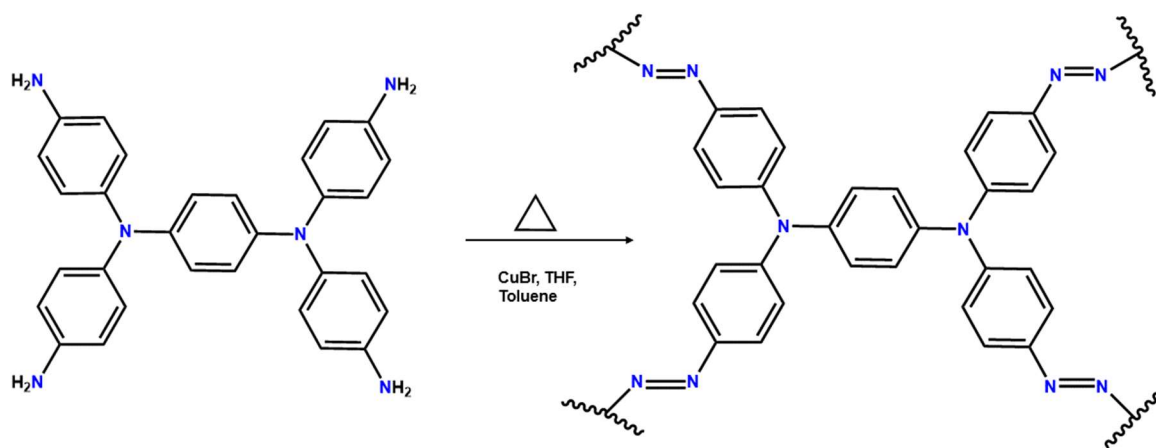
Figure 3.1 Synthesis of azo-linked polymer 6 (ALP-6).

Analysis of the adsorption branch of the nitrogen isotherm led to a BET calculated surface area of 656 m^2g^{-1}. Pore size distribution (PSD) and pre volume were calculated from the adsorption branch using the nonlocal density functional theory (NLDFT). The most dominant pore size was 1.23 nm and the average pore volume was found to be 0.482 cm^3g^{-1}. With the distribution of pores mainly being under 2 nm and the nitrogen uptake isotherm showing a type IV isotherm, it was concluded that this material is microporous in nature.

Analysis of the material by FT-IR was performed and the resulting spectrum was compared to previously published data.[1] Subsequently, FT-IR analysis was performed on the starting material and the disappearance of the bands at 3456 cm^{-1} and 3430 cm^{-1}, corresponding to the asymmetric and symmetric amine stretches, respectively, and the appearance of the shoulder at 1410 cm^{-1}, corresponding to azo (-N=N-) vibration, are indicative of successful polymerization and the complete consumption of starting material.[1]

^{13}C NMR was used to confirm the structural features of the material and was found to be in agreement with previously published data.[1] Power X-ray diffraction analysis was performed and the material was observed to be amorphous in nature. Scanning electron microscopy (SEM) experiments were performed and images confirmed the material's amorphic nature.

After considerable analysis of the material, it was concluded that ALP-6 was successfully synthesized. It was also the aim of this project to investigate the proton conduction behavior of ALP-6. It was the desire of this research team to test the feasibility of this material for use as an acid-doped proton exchange membrane in fuel cell applications.

3.3.2 Acid Doping

The material was subjected to the same doping procedure carried out for the benzimidazole-linked polymers and is illustrated in Figure 3.2. After filtration, it was evident that the doping process was successful; the polymer changed color and texture. The original material was a dark brown fluffy powder with a purple tint. After acid immersion, the material changed to a black chalky substance.
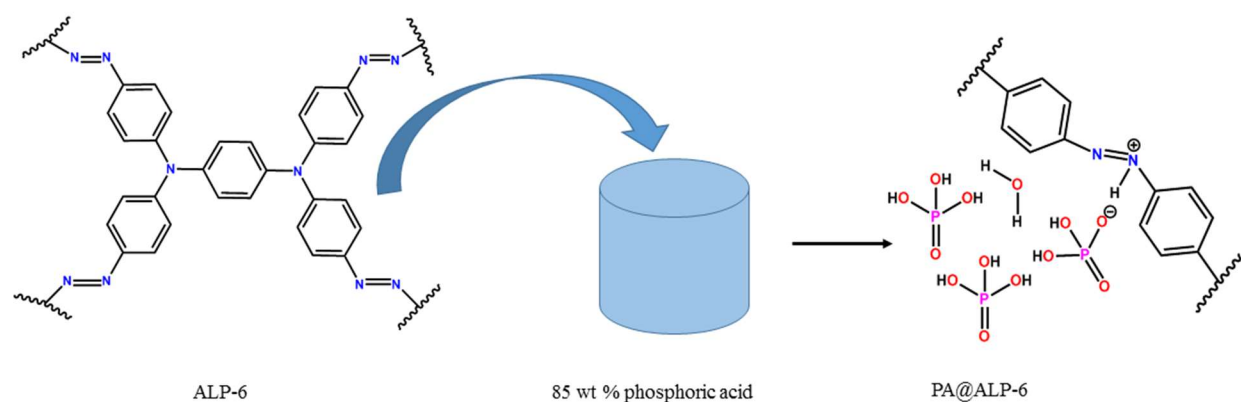
Figure 3.2 Illustration of the doping procedure for ALP-6.

Nitrogen uptake experiments confirmed the integration phosphoric acid into the network (ruling out solely surface modified material) and is shown in Figure 3.3. There is a significant loss in surface area from 656 m^2g^{-1} to 0 m^2g^{-1} and 37 m^2g^{-1} for pristine polymer to the acid embedded material doped with 85 wt% H_3PO_4 and 3 M H_3PO_4, respectively. This can only be explained by the introduction of H_3PO_4 into the polymeric network.
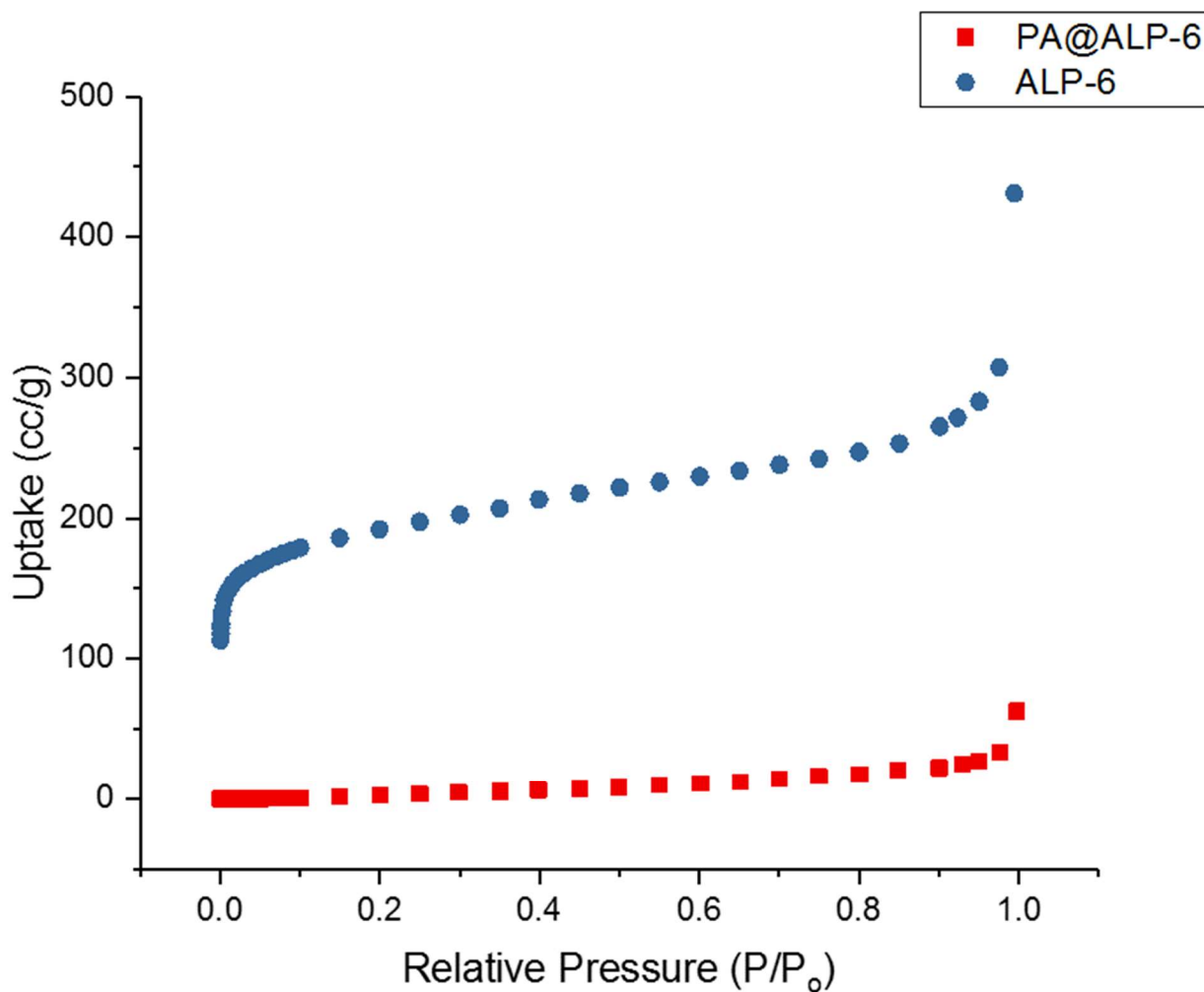
Figure 3.3 Nitrogen uptake isotherms for ALP-6 (blue spheres) and PA@ALP-6 saturated (red). The desorption branches were excluded for visual clarity.

The incorporation of acid into the pores was further confirmed by ^{31}P NMR, FT-IR, and scanning electron microscopy imaging. Figure 3.4 shows a single peak for the doped species and the absence of any similar peak for the pristine material. The presence of one single peak in the NMR spectrum for PA@ALP-6 can be explained by the overwhelming presence of free phosphoric acid. Such high concentrations within the pores masks all other phosphate species,

but further studies of unsaturated polymer can help resolve these peaks.[5] To help elucidate the specific phosphate species within the network, ^{31}P NMR studies were performed on material that was doped with 3M phosphoric acid (all other conditions remained constant), but this was not sufficient to resolve any additional peaks. It should be noted that the phosphorous peak lowered in intensity and grew smaller in area, indicating less phosphoric acid, which correlates with the less concentrated acid used during the doping procedure. The unsaturated material will be referred to as PA@ALP-6 3M throughout the rest of the paper. It is of interest to run 1:1 H_3PO_4 to polymer samples to help with species elucidation.
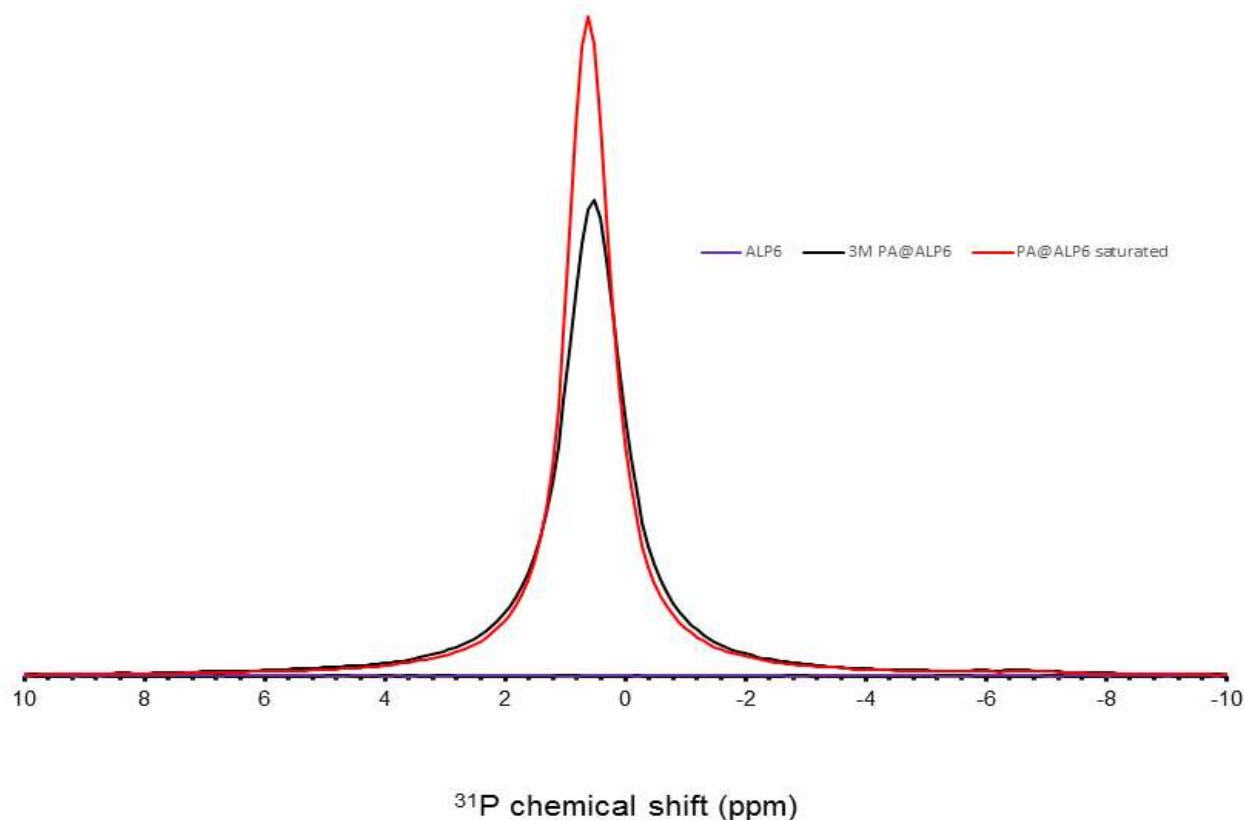
Figure 3.4 ^{31}P NMR spectra overlay of ALP-6 (purple), saturated PA@ALP-6 (red), and PA@ALP-6 doped with 3M H_3PO_4 (black).

Figure 3.5 shows IR spectra of the un-doped and doped, saturated and unsaturated, samples. The appearance of a very broad peak centered at 2750 cm^{-1} is observed for PA@ALP-6 3M, which is indicative of protonation. The peak is shifted slightly upfield to 2728 cm^{-1} for the saturated sample.
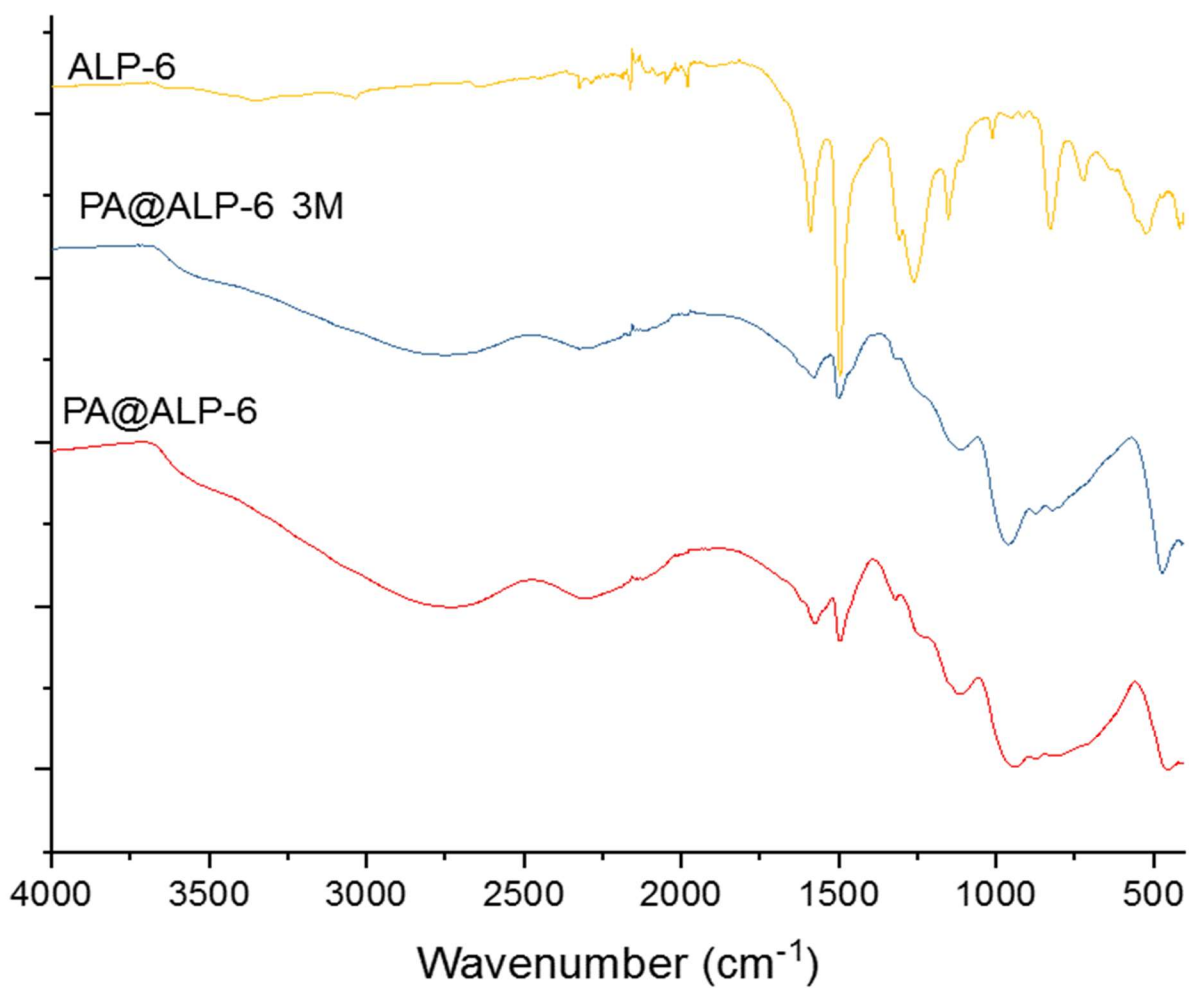
Figure 3.5 FT-IR spectra overlay of ALP-6 (gold), PA@ALP-6 3M (blue), and PA@ALP-6 saturated (red).

SEM images seemed to reveal a change in morphology, but upon closer investigation, the spherical morphology is retained. The material is interconnected by phosphoric acid that resides on the surface and that is interwoven within the network. This binding of aggregates can explain the transformation of the material to a putty-like material, post-doping.
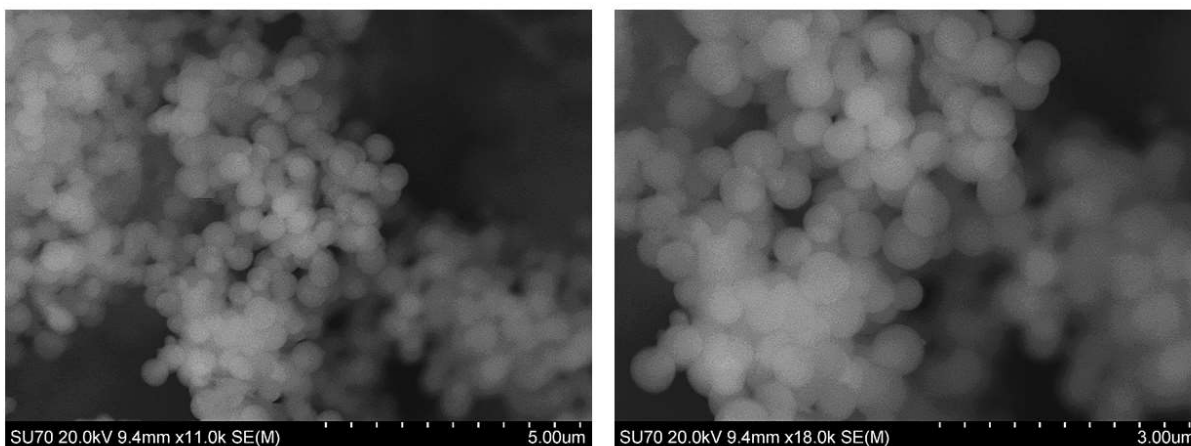
Figure 3.6 SEM images of ALP-6.
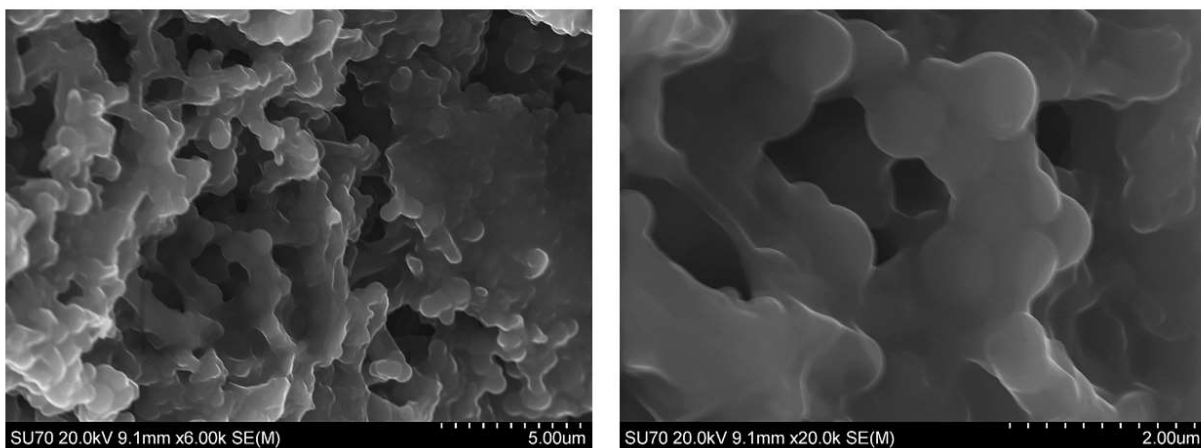
Figure 3.7 SEM images of PA@ALP-6

3.3.3. Phosphate Species

It was one of the aims of this project to understand how the acid is interacting with the polymeric network, which in turn could lend to a better understanding of proton transport behavior. Raman and FT-IR studies were performed on doped samples and the pristine material and the corresponding spectra can be seen in Figures 3.8 and 3.5, respectively.
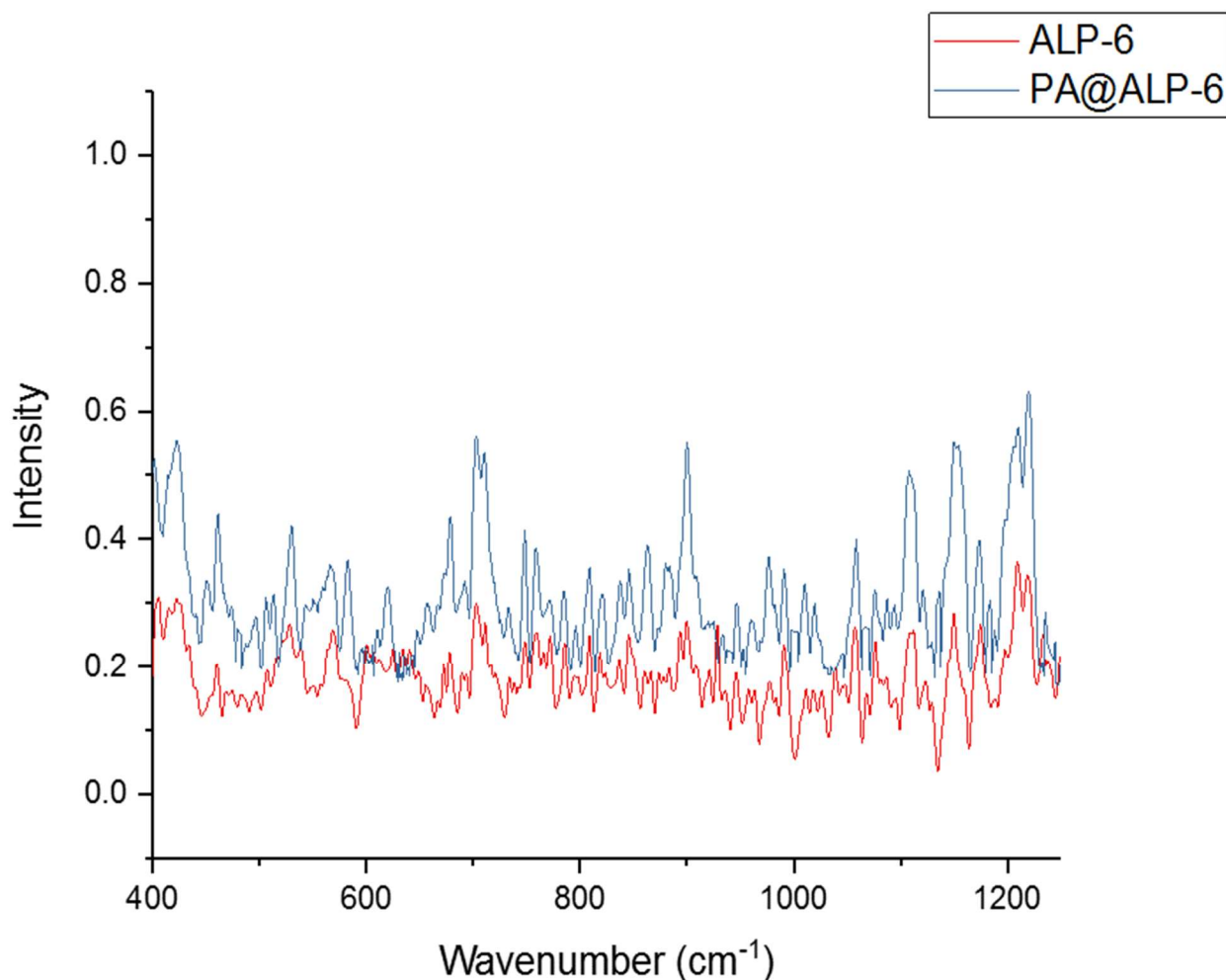
Figure 3.8 Raman spectroscopy overlay spectra of ALP-6 and PA@ALP-6 3M.

Table 3.1 lists the characteristic peaks and gives peak assignments for both Raman and FT-IR vibrations.

Raman		IR		Assignment
ν_{max} (cm^{-1})	Intensity	ν_{max} (cm^{-1})	Intensity	
450	14.7			$\delta_{as}P(OH)_3$
		472	38.8	$\delta(PO_2)$ HPO_4^{2-}
530	42.9			$\delta_s P(OH)_3$
900	84.9			$\nu_s P(OH)_3$
		941	4.7	$\nu(PO)$ H_3PO_4
		1113	23.9	$\nu_s(PO_2)$ $H_2PO_4^-$
1184	4.85			$\nu P=O$

Table 3.1 Characteristic Raman and FT-IR bands for PA@ALP-6 species.

The material was further studied using solid state ^{1}H NMR.
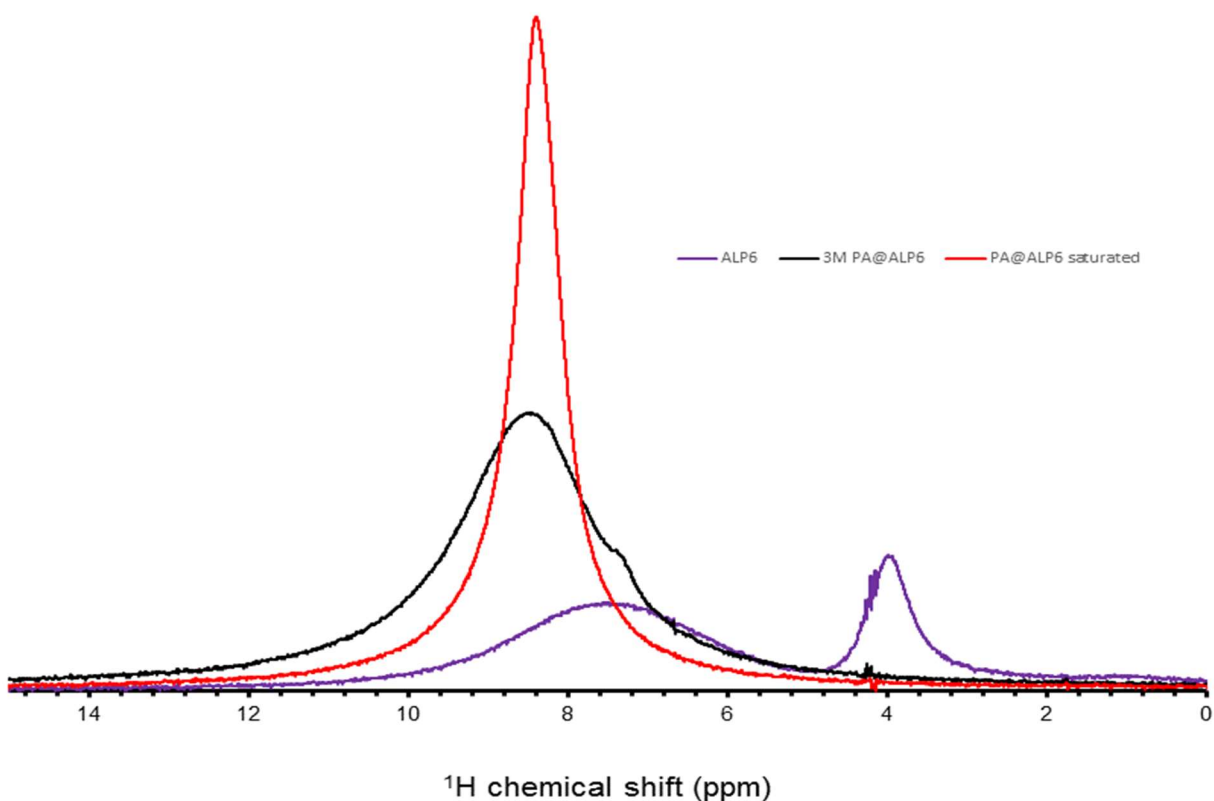
Figure 3.9 ^{1}H NMR overlay spectra of ALP-6 (purple), PA@ALP-6 3M (black), and PA@ALP-6 saturated (red).

3.3.4. Proton Conduction

Quantification of Acid Doping

As previously mentioned, proton conduction is directly proportional to the amount of acid present. The same titration procedure used for PA@BILP-16 (AC) was used to determine the doping level of phosphoric acid within the ALP-6 network. A titration curves is shown below, with analysis of the corresponding data indicating a doping level of 48 moles of H_3PO_4 PRU.
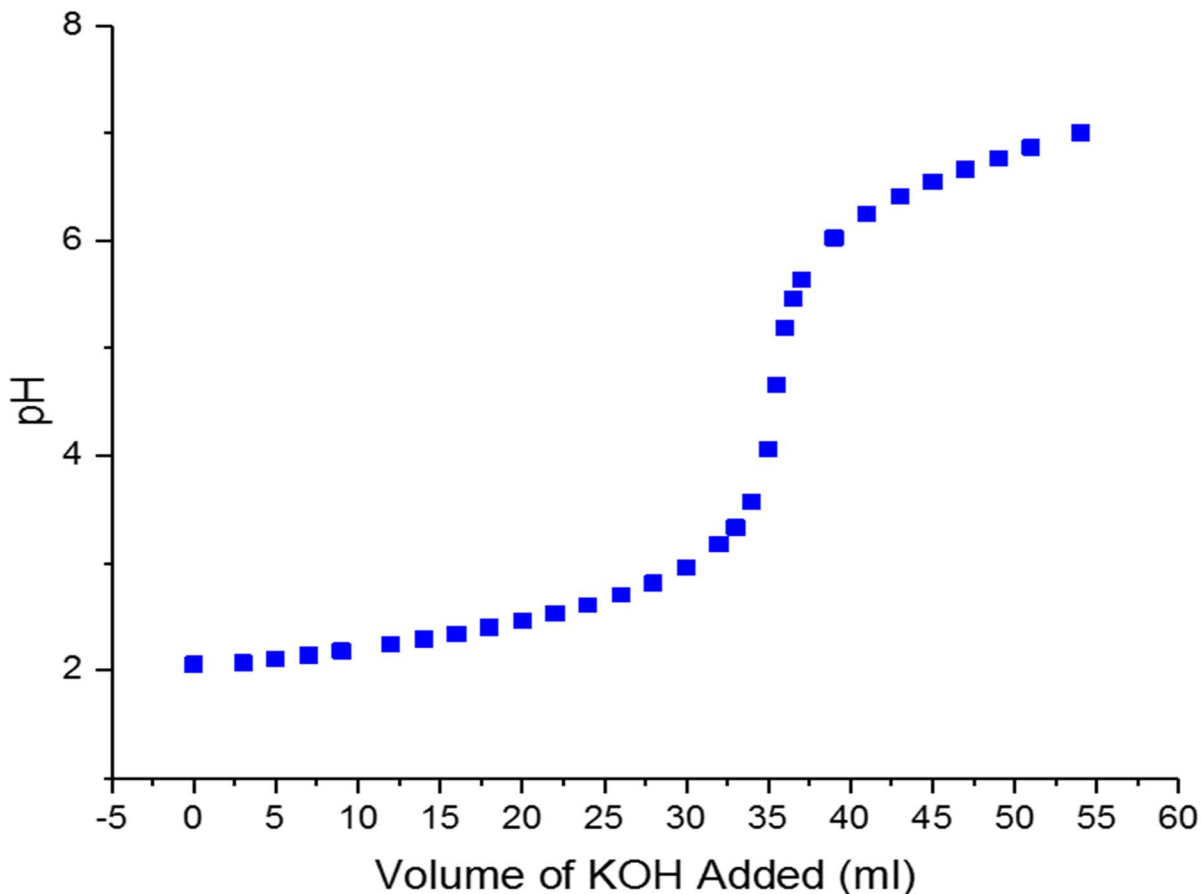
Figure 3.10 Acid/base titration of PA@ALP-6 with 0.1M KOH.

The first equivalence point was determined and the acid content was calculated using Formula 1, where V_{KOH}, C_{KOH}, W_{dry}, and MW represent the volume of the titrant, in this case potassium hydroxide, the concentration of the titrant, the weight of the polymer after drying, and the molecular weight of one repeating unit of the polymer, respectively.

$$Acid\ doping\ level\ = \frac{(V_{KOH})(C_{KOH})}{\left(\frac{W_{dry}}{MW}\right)} \tag{1}$$

The acid content is described as moles of acid per polymer repeating unit (PRU). It was found that ALP-6 was able to achieve an extremely high uptake of 48 moles of phosphoric acid per repeating unit of the polymer.

Additionally, the acid doping level was calculated from the mass of the pristine polymer and the mass of the doped material using Formula 2,

$$Acid\ doping\ level = \frac{W_d}{W_i} \cdot \frac{M_{w-ALP}}{M_{w-H3PO}} \tag{2}$$

Where W_d, W_i, M_{w-ALP6} and $M_{w-H3PO4}$ are the difference in masses between the doped and pristine material, the initial mass of the undoped polymer, the molecular weight of a single repeating unit of ALP-6, and the molecular weight of phosphoric acid, respectively.[6] From the above equation, it was found that the doping level of ALP-6 with 85 wt% H_3PO_4 and 3 M H_3PO_4 was found to be 36.27 and 19.79, respectively. The increase in weight from pristine to doped material for 3 M and saturated PA@ALP-6 were found to be 487% and 816%, respectively. It should be noted that these values take into account any adsorbed water. Further experiments can isolate the acid doping from the water doping. Taking into consideration the water doping, these values correlates well with previously published data on linear PBI samples doped with phosphoric acid.[7]

Thermogravemetric analysis experiments were performed on the saturated, 3M, and pristine material.
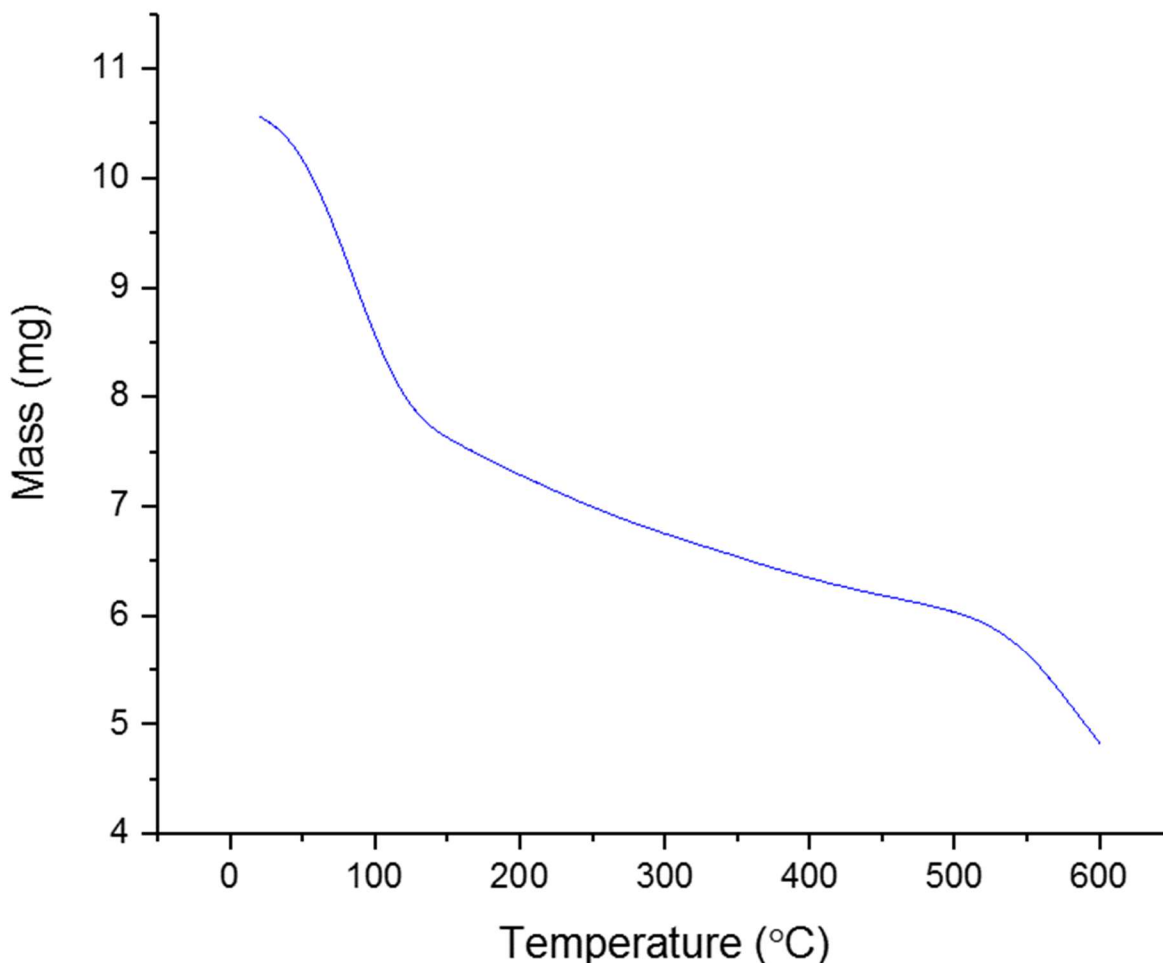
Figure 3.11 TGA spectrum of PA@ALP-6.

From figure 3.11 it was observed that there is an intial weight loss of 1.54 mg (~15 wt%), corresponding to the evaporation of water. This correlates well with the fact that 85 wt% H_3PO_4 was used for this study. There is a second weight loss that is more gradual, starting ~120 °C, which corresponds to the dehydration/polymerization of phosphoric acid. The weight loss during this second stage is roughly 2.92 mg. This weight loss and the weight loss due to water, coupled together, account for only roughly 40% of the weight loss. This is not in agreement with other techniques and most likely is due to the polymerization of phosphoric acid and the

resulting intercalation. Total weight loss of the original acid is not seen until the material completely decomposes.

Analysis of the material using energy dispersive X-ray spectroscopy confirmed the ability of the material to adsorb such high amounts of acid. Although this technique does not be directly correlate, it does give insight into acid loading and support previous findings. Figure 3.12 shows an overwhelming phosphorous peak of around 3,000 counts at ~ 2.0 kEV compared to a carbon peak of only around 1,000 counts. There are 32 carbon atoms per repeating unit in ALP-6 and 1 phosphorous atom per molecule of acid. The EDS quantative results show a carbon composition that is six times higher than phosphorous, but taking into account the previous statement and the fact Figure 16 is for an unsaturated sample, this is a monstrous amount of acid embedded in the material. It should be noted that the Al and Ag peaks are not derived from the sample. Due to the electron insulating character of ALP-6, a conductive material must be used to analyze the material. These results quantified the amount of acid that was impregnated into the material and indicated that PA@ALP-6 has strong potential for use as an acid-doped PEM.
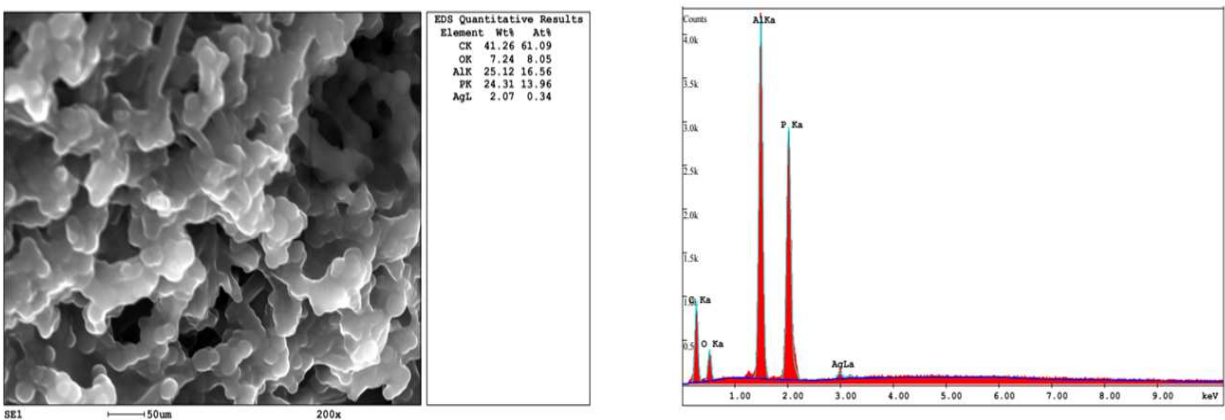
Figure 3.12 EDX spectrum for PA@ALP-6 (right) and EDS quantitative results for elemental composition (left).

Electrochemical Impedance Spectroscopy

Preparation of the PA@ALP-6 membrane for testing followed the same pelletization process and incorporation into the fuel cell for quasi four probe *ex-situ* studies. The same parameters previously reported were imployed and 3 separate experiments were performed to insure reproducibility. The resulting spectra are pictured below.
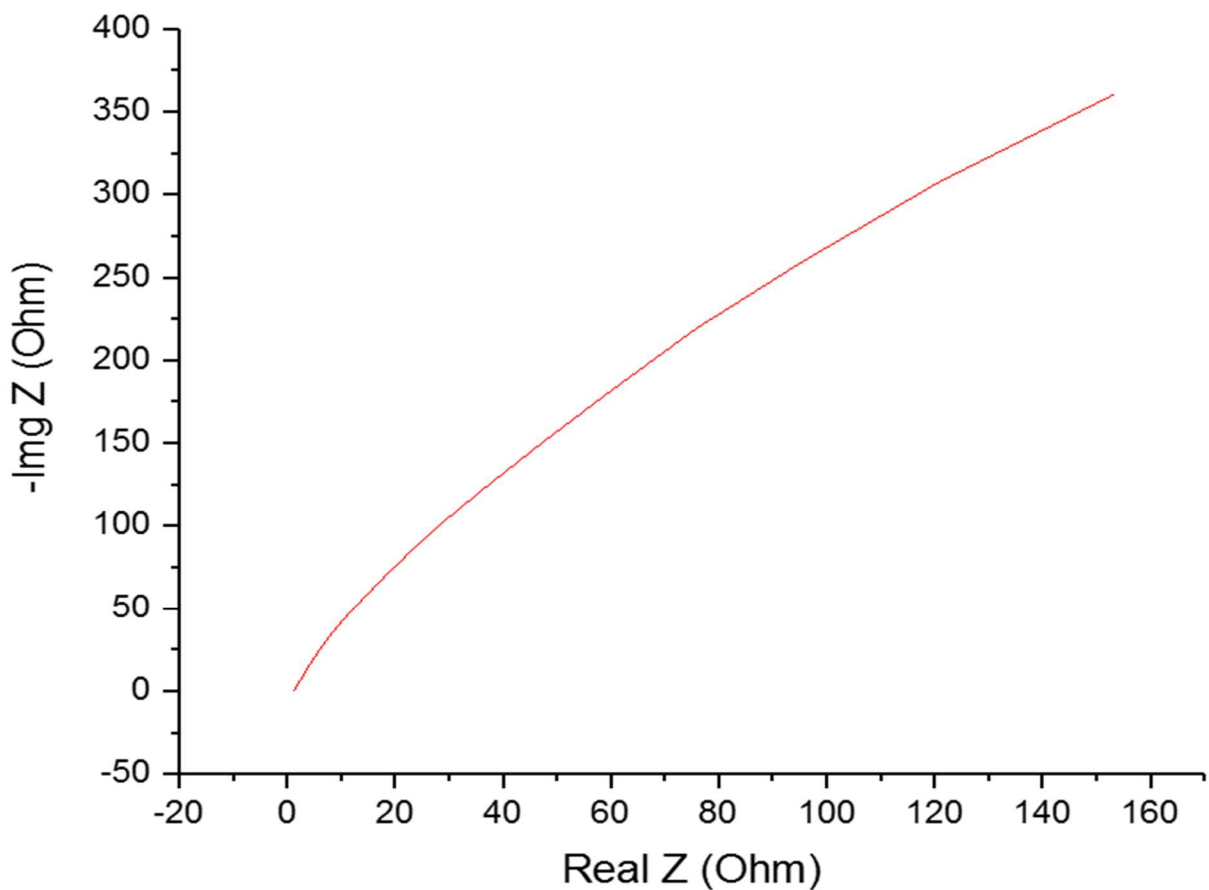
Figure 3.13 EIS spectrum of PA@ALP-6 at 23 °C.

The ohmnic resistance was calculated from the intersection of the plot against the real axis (x-axis) in the high frequency region. Figure 3.13 shows the elctrochemical impedance spectroscopy spectrum (EIS) for PA@ALP-6 at room temperature and anhydrous conditions and Formula 1 was used to obtain a proton conduction value of 5.91 S·cm^{-1} for

$$\sigma = \frac{L}{R \cdot A} \qquad (3)$$

PA@ALP-6, where σ is proton conduction, L represents pellet thickness (in cm), R is the resistance, and A is the area of the pellet. Taking into account the fact that these studies were peformed under anhydrous and ambient conditions, this value strongly competes with top performing materials to date and these competing materials are listed in Table 3.2. It is worth noting that PA@ALP-6 slightly outperformed PA@BILP-16 (AC) under similar conditions. This can be explained by a increase in surface area of roughly 60 m^{2}g^{-1} for ALP-6 over BILP-16 (AC), which, in turn, led to a slightly improved acid uptake. The higher amount of acid adsorbed into the system allowed for higher proton conduction values.

	Compound	Conductivity (Scm^{-1})	Conditions	Reference
1	Nafion®	~1 × 10^{-1}	80°C, 98% RH	*J. Polym. Sci., Part B: Polym. Phys.* 2011, 49, 1437
2	H$_3$PO$_4$@ALP-6	5.91 x 10^{-2}	60°C, 0% RH	*This Work*
3	H$_3$PO$_4$@BILP-16 (AC)	5.8 x 10^{-2}	60°C, 0% RH	*This Work*
4	H$_3$PO$_4$@PBI	5 × 10^{-2}	60°C, 0% RH	*Chem. Mater.*, 2005, 17, 21, 5329
5	SPEEK	2 × 10^{-2}	80°C, 98% RH	*J. Polym. Sci., Part B: Polym. Phys.* 2011, 49, 1437
6	H2SO4@MIL-101	6.0 × 10^{-2}	80°C, 20% RH	*J. Am. Chem. Soc.* 2012, 134, 15640
7	H$_3$PO$_4$@MIL-101	3 × 10^{-3}	150°C, 0.13% RH	*J. Am. Chem. Soc.* 2012, 134, 15640
8	PA@Tp-Azo	9.9 × 10^{-4}	25°C, 98% RH	*J. Am. Chem. Soc.* 2014, 136, 6570

Table 3.2 Top performing materials for PEMs.

The dependence of proton conductivity for PA@ALP-6 on temperature was also investigated and the results are displayed in Figure 3.14. Experiments were run in the temperature range of 25 °C to 83 °C, with proton conductivity values reaching their highest levels at 83°C.
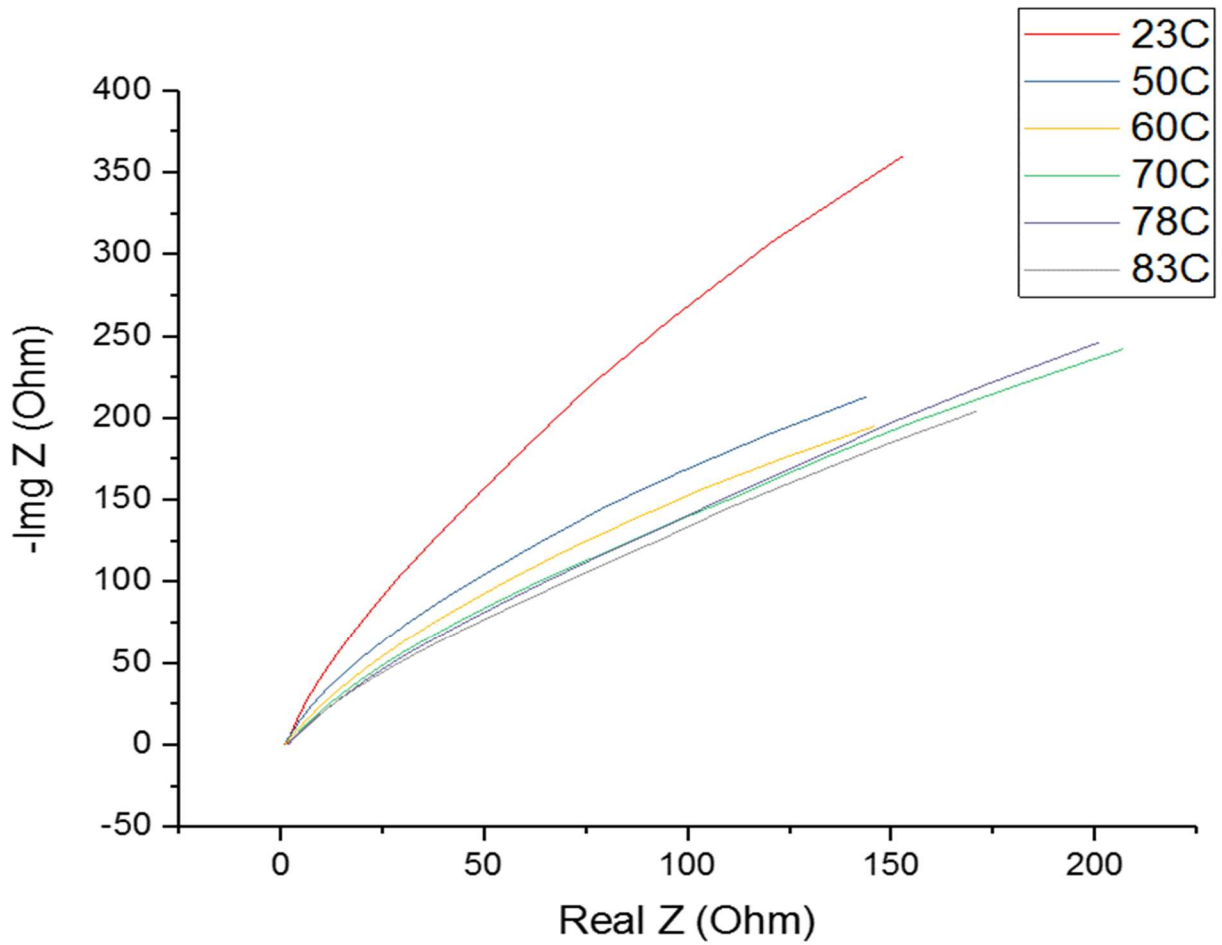
Figure 3.14 EIS spectra overlay for PA@ALP-6 at varying temperatures.

Materials similar to PA@ALP-6 that exhibit a hoping-like proton conduction mechanism, the temperature dependent proton conductivity can be expressed by equation (4)

$$\sigma = \sigma_o^{\frac{E_a}{RT}} \tag{4}$$

where σ is the proton conductivity, σ_o is the pre-exponential factor, E_a is the activation energy, T is the temperature, and R is the ideal gas constant.[9]

This assumes that there is no change in concentrations along the temperature range studied. This is problematic due to the fact a loss in water was observed at temperatures above 60 °C. So, there is an increase in conductivity observed up to said temperature, followed by a decrease in conductivity caused by the loss of water. This drop in conductivity does occur infinitely, but instead, above 85 °C, an increase in conductivity was observed. This resulted from an increase in kinetics and can be explained using equation 3, but can be better explained using the Arrhenius plot of conductivity.

3.4 Conclusions

It has been successfully demonstrated that azo-linked polymers can play a role in fuel cell applications by doping them with mineral acid for use as proton exchange membranes. The high porosity, high pore volume, and high nitrogen content (Lewis basic sites) allow for high acid uptake. Upon saturation of the material with phosphoric acid, a high proton conductivity value of 5.91×10^{-2} S/cm can be achieved at 60 °C. With its high thermal and chemical stability and the observed facile proton conduction, the material should be optimized via structure-property relationships and *in-situ* studies should be subsequently executed.

Chapter 3 References

1. Arab, P.; Parrish, E.; Islamoglu, T.; El-Kaderi, H. M. *J. Mater. Chem. A.*, **2015**, *3*, 20586-20594.

2. Rudolph, W. *Dalton Trans.*, **2010**, *39*, 9642-9653.

3. Okamoto, H.; Hamaguchi, H.; Tasumi, M. *Chemical Physics Letters*. **1985**, *130*, 185-189.

4. Stuart, C.; Frontiera, R.; Mathies, R.; *J. Phys. Chem.* **2007**, *111*, 12072-12080.

5. Schechter, A.; Savinell, R.F.; Wainright, J.S.; Ray, D. *Journal of the Electrochemical Society*. **2009**, *156,* B283-B290.

6. Ergun, D.; Devrim, Y.; Bac, N.; Eroglu, I. *Journal of Applied Polymer Science*. **2012**, *124*, E267-E277.

7. Q. Li, R. He, J. O. Jensen and N. J. Bjerrum, *Fuel Cells*, 2004, **4**, 147–159.

8. Chandra, S.; Kundu, T.; Kandambeth, S.; BabaRao, R.; Marathe, Y.; Kunjir, S.M.; Banerjee, R. *J. Am. Chem. Soc.* **2014**, *136*, 6570-6573.

9. Bruce, P. G. *Solid state electrochemistry*; Cambridge Univ. Press: Cambridge, 1995.

Chapter 4

Concluding Remarks

Herein, two new classes of polymers were investigated for use as proton exchange membranes to aid in developing state of the art fuel cells. Both polymers, BILP-16 (AC) and ALP-6, exhibit high porosity, high pore volume, high chemical and thermal stability, and high nitrogen content. These characteristics, coupled with their relative inexpensive and easy synthetic routes, have made them attractive in the areas of gas storage and gas separation. To the best of my knowledge, to date, these materials have not been investigated for use in fuel cell applications.

This work was inspired by the use of other porous materials (i.e. MOFs and COFs) and linear analogues of the benzimidazole materials in fuel cell applications. It was the hypothesis of the overall project that these new classes of polymers would utilize the advantageous attributes of previously studied porous materials, while circumventing the problematic traits. It was also hypothesized that the lack of crystallinity in BILPs and ALPs would not significantly hinder these materials' ability to facilitate proton mediation in an effective and efficient manner.

Both materials proved to be viable options for use as PEMs with the acid-doped azo-linked polymer (PA@ALP-6) exhibiting slightly higher proton conductivity values under equivalent conditions. Proton conductivity values reached 5.80×10^{-2} S/cm and 5.91×10^{-2} S/cm at 60 °C and 0% relative humidity for PA@BILP-16 (AC) and PA@ALP-6, respectively. Acid-base titrations, TGA experiments, and acid uptake experiments were performed to quantify the amount of acid embedded into the networks. It was determined that these materials can adsorb extremely high amounts of H_3PO_4 into its matrix through two different means; (1) anchoring of

phosphoric acid at basic nitrogen sites and (2) hydrogen bonding through phosphate-phosphate interactions and hydrogen bonding through phosphate-polymer interactions. With no change in morphology and excellent chemical and thermal stability (stable up to ~400 °C), even after doping with >14 M acid, these materials should easily withstand the harsh conditions of fuel cell environments. There is still much to learn about the proton mediation behavior of these materials, as well as the acid-matrix interactions, but the studies listed in this thesis shed light on a promising material, not previously studied for fuel cell applications.